Water Science & Technology

Water Science & Technology Vol 00 No 0, 1 doi: 10.2166/wst.2022.318

Synthesis characterization of Zn-based MOF and their application in degradation of water contaminants

Saade Abdalkareem Jasim[a], Hawraz Ibrahim M. Amin[b,c], Ahmad Rajabizadeh[d,e], Marcos Augusto Lima Nobre[f], Fariba Borhani[g,*], Abduladheem Turki Jalil[h], Marwan Mahmood Saleh[i], Mustafa M. Kadhim[j,k] and Mehrdad Khatami[l]

[a] Medical Laboratory Techniques Department, Al-Maarif University College, Al-Anbar-Ramadi, Iraq
[b] Chemistry Department, Salahaddin University-Erbil, Erbil, Iraq
[c] Department of Medical Biochemical Analysis, Cihan University-Erbil, Erbil, Iraq
[d] Environmental Health Engineering Research Center, Kerman University of Medical Sciences, Kerman, Iran
[e] Department of Environmental Health Engineering, Faculty of Public Health, Kerman University of Medical Sciences, Kerman, Iran
[f] School of Technology and Sciences, São Paulo State University (Unesp), Presidente Prudente, SP 19060-900, Brazil
[g] Medical Ethics and Law Research Center, Shahid Beheshti University of Medical Sciences, Tehran, Iran
[h] Medical Laboratories Techniques Department, Al-Mustaqbal University College, Babylon, Hilla 51001, Iraq
[i] Department of Biophysics, College of Applied Sciences, University of Anbar, Ramadi, Iraq
[j] Department of Medical Laboratory Techniques, Dijlah University College, Baghdad 10021, Iraq
[k] Medical Laboratory Techniques Department, Al-Farahidi University, Baghdad, Iraq
[l] Department of Medical Biotechnology, Faculty of Medical Sciences, Tarbiat Modares University, Tehran, Iran
*Corresponding author. E-mail: faribaborhani@msn.com

MK, 0000-0002-7519-6998

ABSTRACT

Metal-organic frameworks (MOFs) are currently popular porous materials with research and application value in various fields such as medicine and engineering. Aiming at the application of MOFs in photocatalysis, this paper mainly reviews the main synthesis methods of ZnMOFs and the latest research progress of ZnMOFs-based photocatalysts to degrade organic pollutants in water, such as organic dyes. This nanomaterial is being used to treat wastewater and has proven to be very efficient because of its exceptionally large surface area and porous nature. The results show that Zn-MOFs are capable of high degradation of the above pollutants and over 90% of degradation was observed in literatures. In addition, the reusability percentage was examined and studies showed that Zn-MOFs nanostructure has very good stability and can continue to degrade a high percentage of pollutants after several cycles. This review focuses on Zn-MOFs and their composites. First, the methods of synthesis and characterization of these compounds are given. Finally, the application of these composites in the process of photocatalytic degradation of dye pollutants such as MB, methyl orange (MO), crystal violet (CV), RhB, etc. is explained.

Key words: environmental health, metal-organic framework, methylene blue, photocatalyst degradation, water pollutants

HIGHLIGHTS

- The performance of Zn-MOFs enhanced photocatalytic activity by scavenging entire chemicals and water pollutant.
- Zn-MOFs are capable of high degradation of the above pollutants and over 90% of degradation.
- MOFs nanostructure has very good stability and can continue to degrade a high percentage of pollutants after several cycles.

GRAPHICAL ABSTRACT

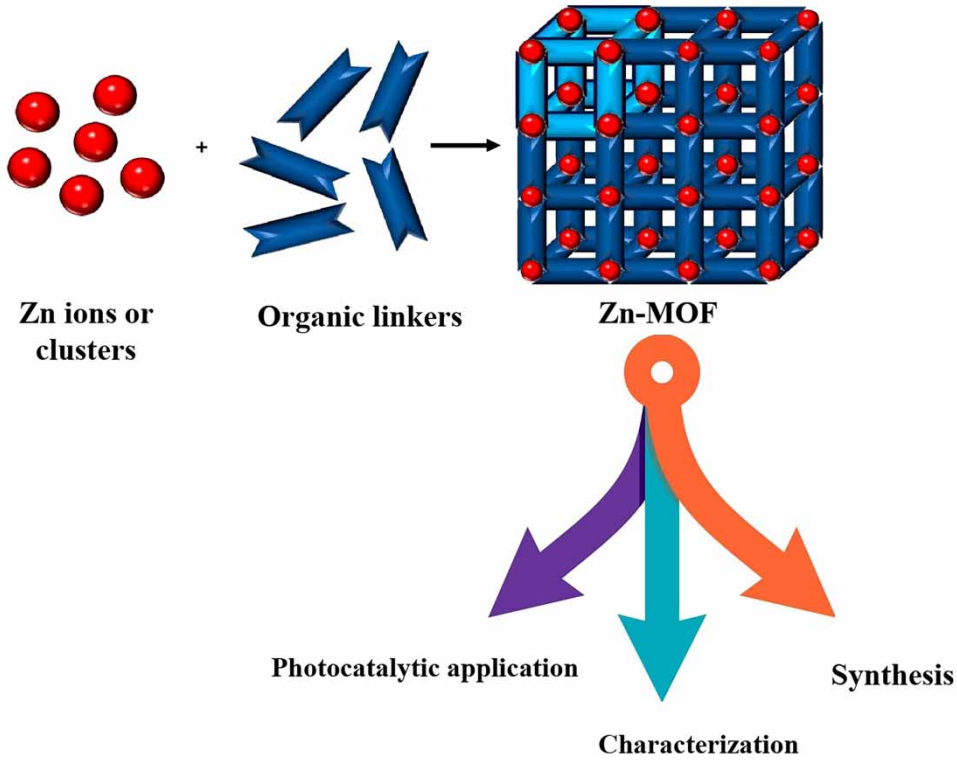

LIST OF ABBREVIATIONS

MOFs	Metal-organic frameworks
NC	Nanocomposite
MB	Methylene blue
RhB	Rhodamine B
MV	Methyl violet
MO	Methyl orange
CV	Crystal violet
RY 145	Reactive Yellow 145
2-CP	2-chlorophenol
DMF	Dimethylformamide
BDC	Benzene-1,4-dicarboxylate
FT-IR	Fourier transform infrared
XRD	X-ray diffraction
SEM	Scanning electron microscope
EDS	Energy-dispersive X-ray spectroscopy
DRS	Diffuse reflection spectroscopy
TEM	Transmission electron microscopy
GO	Graphene oxide
BET	Brunauer–Emmett–Teller spectroscopy
SAED	Selected area electron diffraction
TGA	Thermogravimetry
XPS	X-ray photoelectron spectroscopy

1. INTRODUCTION

Exterior contaminants, evaporation, and a complete absence of tap water were all cited as major cultural problems in recent years (Emam *et al.* 2020; Liu *et al.* 2020; Roostaee & Sheikhshoaie 2022a). Furthermore, water quality has deteriorated

dramatically in recent years as a result of growing urbanization, worldwide industrialization, and population growth, causing serious difficulties for microorganisms and humans (Liu *et al.* 2008; Zhang *et al.* 2021a). Different industrial activities released large amounts of extra effluent into the ecosystem, resulting in severe environmental contamination (Liu *et al.* 2021a; Tan *et al.* 2022a). For instance, industrial effluents with a toxic effect, such as benzene, phenols, antibiotics (Chen *et al.* 2022), and dyes with high toxicity and difficult degradability, might infect sea life and the environment (Chen *et al.* 2021a; Fauzi *et al.* 2022). Generally, natural and synthetic/artificial dyes are the two main types of dyes. Plants source provide natural dyes, such as lichens, fungus, woods, fruits, leaves, roots, bark, and lichens while chemical dyes, earth minerals, and petroleum compounds were used to create artificial dyes. Synthetic dyes are usually employed in dyestuff and printing processes in sectors such as textiles, leather, cosmetics, and papers, owing to the high demand for individualization (Roostaee & Sheikhshoaie 2022a). On the other hand, textile colors and some other chemical dyes, are extremely easily combined with freshwater resources from other sectors. Furthermore, due to the highly hazardous chemical compounds included in these dyes, they can be regarded as serious water pollutants (Senthil *et al.* 2019). The dye may be the first toxin discovered in sewage. It is well acknowledged that the dye has a significant impact on popular estimates of the quality of water. As a result, creating an effective technique to eliminate contaminants from wastewater is critical, and researchers around the world are paying special attention to this problem (Firouzeh *et al.* 2021; Ghazal *et al.* 2021).

Semiconductor photocatalytic technology has shown significant potential in the degradation of pollutants in recent years (Guo & Wang 2019). However, traditional photocatalysts which were among the first investigated photocatalyst can only utilize ultraviolet. To date, numerous novel visible-light-driven semiconductor photocatalysts have been explored to overcome the drawbacks of existing catalysts and further advance photocatalytic technology. Photocatalysts are the heart of photocatalytic technology, which has gained popularity as a green method for the total degradation of organic pollutants utilizing a freely available solar energy source without emitting any secondary pollution (Wen *et al.* 2020; Bai *et al.* 2021). Today, various sciences (Alimadadi *et al.* 2019; Volodymyr *et al.* 2021; Akter *et al.* 2022) such as environment (Alshehrei *et al.* 2021; Wang *et al.* 2021a; Awad *et al.* 2022; Dai *et al.* 2022a), engineering (Assi *et al.* 2021; Hussein *et al.* 2021; Li *et al.* 2021a; Majdi & Vacareanu 2021), computer (Liu *et al.* 2021b), agriculture (Tian *et al.* 2021a, 2021b; Wang *et al.* 2022a), chemistry (Ge *et al.* 2019; Liu *et al.* 2020; Qin *et al.* 2022), physics (Li *et al.* 2022a), and medicine (Chen & Wang 2021; Endriani *et al.* 2022; Kausikan *et al.* 2022; Mahawar *et al.* 2022; Zheng *et al.* 2022) have made significant progress (Amiri *et al.* 2020; Chu *et al.* 2020; Zhao *et al.* 2020a, 2021a, 2021b, 2021c, 2021d; Nazeer *et al.* 2022; Rashid *et al.* 2022a; Zhao *et al.* 2022a, 2022b). Nanoscience is no exception to this rule (Barani *et al.* 2020; Bilal *et al.* 2020; Chu *et al.* 2021; Sargazi *et al.* 2021; Salarpour *et al.* 2022). Nanoparticles such as nanocubes (AlYahya *et al.* 2018), nanotube (Gao *et al.* 2021; Jasim *et al.* 2022a), nanocages (Salahdin *et al.* 2022), nanofibrous (Jasni *et al.* 2017), nanomagnetic (Akbarizadeh *et al.* 2022a; Cao *et al.* 2022; Jasim *et al.* 2022b; Sadeghi *et al.* 2022), nanorods (Isacfranklin *et al.* 2020a, 2020b), chain like (Swathi *et al.* 2020), nanoplates (Vidhya *et al.* 2021), nanoporous (Yang *et al.* 2019a), bimetallic (Cao *et al.* 2021a; Ameen 2022), titanium (Ahmed *et al.* 2020), silver (Ameen *et al.* 2018, 2019, 2020a, 2020b, 2021a; Kim *et al.* 2018; Mohanta *et al.* 2018; Mythili *et al.* 2018a; Valarmathi *et al.* 2020; Rajadurai *et al.* 2021; Almansob *et al.* 2022a; Begum *et al.* 2022), tin oxide (Al-Enazi *et al.* 2021; Wang *et al.* 2022b), gold (Iram *et al.* 2017; Mythili *et al.* 2018b; Rahim *et al.* 2018; Alsamhary *et al.* 2020), selenide (Naveenraj *et al.* 2018), zinc oxide (Saravanan *et al.* 2018; Ameen *et al.* 2021b), copper (Ghodake *et al.* 2018; Sonbol *et al.* 2021a; Indhira *et al.* 2022), chromium (Isacfranklin *et al.* 2020c), graphene (Khan *et al.* 2020), palladium (Sonbol *et al.* 2021b), nickel (Moghadam *et al.* 2022; Nazaripour *et al.* 2022), barium (Hashemi *et al.* 2021) nanoparticle (Roostaee & Sheikhshoaie 2020; Aljumaily *et al.* 2022; Cao *et al.* 2022; Xia *et al.* 2022), capped/doped (Rao *et al.* 2018; Begum *et al.* 2021; Cao *et al.* 2021b; Akbarizadeh *et al.* 2022b; Haghighat *et al.* 2022), core-shell (Khatami *et al.* 2018; Shafiee *et al.* 2022), MOF (Alahri *et al.* 2021), COF, carbon fiber (Gao *et al.* 2022), etc (Almansob *et al.* 2022b; Ameen *et al.* 2022; Megarajan *et al.* 2022), are important category of materials that can be explored to various applications (Jia *et al.* 2014; Guo *et al.* 2017; Gao *et al.* 2019; Xin *et al.* 2021; Yang *et al.* 2021a; Chu *et al.* 2022a; Li *et al.* 2022b; Mohammed *et al.* 2022; Zhang *et al.* 2022). This material uses in many fields such as drug delivery (Barani *et al.* 2021a, 2021b; Obireddy & Lai 2021; Rabiee *et al.* 2021; Zha *et al.* 2021), antioxidant (Gangalla *et al.* 2021), energy deposition (Yang *et al.* 2021b), sickness treatment (Chen *et al.* 2021b), removal (Yang *et al.* 2019b), photo-catalyst (Khatami & Iravani 2021; Al-Nayili *et al.* 2022; Selvam *et al.* 2022; Shafiee *et al.* 2022), corrosion (Li *et al.* 2022c), green manufacturing (Zhang *et al.* 2018a; Wu *et al.* 2021), antibacterial (Arkaban *et al.* 2022; Mortezagholi *et al.* 2022; Nazaripour *et al.* 2022; Subramaniyan *et al.* 2022), antifungal (Mostafa *et al.* 2020; Sarika *et al.* 2021), sensors and biosensors (Nazari-Vanani *et al.* 2019; Alhomaidi *et al.* 2022; Roostaee & Sheikhshoaie 2022b, 2022c; Roostaee *et al.* 2022), batteries (Rajabizadeh *et al.* 2022), microgrinding (Li *et al.*

2016; Zhang *et al.* 2017; Yang *et al.* 2021c; Jia *et al.* 2022), biomedical (Alijani *et al.* 2021; Raeisi *et al.* 2021) and so on (Kumar *et al.* 2022). Metal-organic frameworks (MOFs) are one of the most widely used and important of these nanostructures (Safaei *et al.* 2019; AlNadhari *et al.* 2021).

For a variety of uses, such as gas sorption and separation, sensing devices, photocatalytic degradation, and drug carriers, MOFs with enormous surface areas, homogeneous catalyst surfaces, extendable enormous porosity size, and highly ordered tunable pore were evaluated (Abdelhameed & Emam 2022; Abdelhameed *et al.* 2022). One of the most important applications that have found many enthusiasts today is the use of MOFs in photocatalytic degradation (Zhang *et al.* 2021b; He *et al.* 2022). Metal-organic frameworks, a new class of porous crystalline materials, have piqued the interest of researchers due to their amazing properties such as large surface area, crystallinity, and controllable porosity, as well as their extensive application potential (Bazi Alahri *et al.* 2021; Zhu *et al.* 2022). Garcia *et al.*'s research proved that MOF-5 had both great potential for applications and catalytic performance (Abdelhameed *et al.* 2021a; Emam *et al.* 2021). Ever since, the catalysts removal of organic contaminants using MOFs as photocatalysts has gained popularity as a proposed study (Abdelhameed *et al.* 2021b). In contrast to traditional porous substances, MOFs can be made in a more controlled environment that enhances stability, and by changing individual components, it is possible to thoroughly develop the physicochemical properties. Currently, organic pollutant listeria is being reduced by using photoactive MOFs that function as photocatalysts (Ebrahimi *et al.* 2018; Abdelhameed *et al.* 2021c). Photoactive MOFs have the following benefits over traditional inorganic photocatalysts: (1) The intrinsic porosity of the material can let organic contaminants and chemicals diffuse via open channels, and that is critical for photocatalytic degradation performance, (2) Because of the modular nature of MOF produced, this new class of photocatalysts can be rationally designed and fine-tuned at the molecular scale, allowing the electrical structure of MOF photocatalysts to be readily modified, (3) Various synthetic methods, such as vapor diffusion, solvothermal approach, ultra-sonication, and emulsion-assisted precipitation, enable MOF photocatalysts to have excellent crystalline quality and morphologies (Zhang *et al.* 2018b).

With various advances in mathematics, physics, chemistry, biology, medicine, and other sciences (Amiri *et al.* 2021a, 2022; Rezapour *et al.* 2021; Ashpazzadeh *et al.* 2022; Chu *et al.* 2022b; Iqbal *et al.* 2022; Qian *et al.* 2022; Zhao *et al.* 2022c, 2022d), the removal of contaminants from water is not impossible (Liu *et al.* 2018; Dai *et al.* 2022b), and as mentioned, it has various solutions, including photocatalytic degradation. When exposed to UV and visible irradiation, a small percentage of Zn-MOFs or Zn coordination polymers were examined for photocatalytic destruction of organic molecules (Tian *et al.* 2021c). Under visible light illumination, three Cd and two Zn coordination polymers showed relatively significant photocatalytic performance in the destruction of methylene blue (MB), according to the Liu and Ma group. Wang's group produced two Zn and two Cd coordination polymers based on the thiophene-pyridyl-amine ligand for photocatalytic MB degradation under UV–Vis illumination (Wang *et al.* 2017). When exposed to UV light, the Zhang group developed a Zn coordination polymer containing 2,4,5 tri(4-pyridyl)-imidazole and naphthalene-1,5-disulfonate, which displayed strong photocatalytic performance for the decomposition of rhodamine B (RhB) (Wang *et al.* 2018a). The Zn-MOFs with 1,4-bis(triazol-1-yl)terephthalic acid ligand displayed photocatalytic degradation of methyl violet (MV) and RhB when exposed to UV light. according to Ma, Liu, and Kumar (Jin *et al.* 2018).

This review focuses on Zn-MOFs and their composites. First, the methods of synthesis and characterization of these compounds are given. Finally, the application of these composites in the process of photocatalytic degradation of dye pollutants such as MB, methyl orange (MO), crystal violet (CV), RhB, etc. is explained.

2. STRUCTURE OF ZN-MOFS

As noted previously, the controllable characteristics of the composites produced as a result of the preparation of MOF catalysts have attracted considerable interest over the past few decades. Zn-MOFs, one of these compounds, have a variety of characteristics, including high specific surface areas, tunable sizes, and suitable energy band gaps. As a consequence, it might lead to improved behavior in a variety of uses (Safaei *et al.* 2019).

Manna *et al.* (2018) synthesized Zn(II)-Based MOF. This metal-organic framework was created via gradual diffusion of the ligand L and $ZnSiF_6$ at room temperature, resulting in block-shaped yellow crystals. This group investigated the structure of prepared Zn-MOFs. The asymmetric component is made up of a SiF_6^{2-} anion, two linkers, and Zn(II) metal ion, with dichloromethane and some other disorganized compounds filling the voids (Figure 1(a)). The Zn(II) metal terminal is octahedrally coordinated with the N_4F_2 donor, with the spacing between Zn(II) and equatorial nitrogen atoms being 2.139 while the

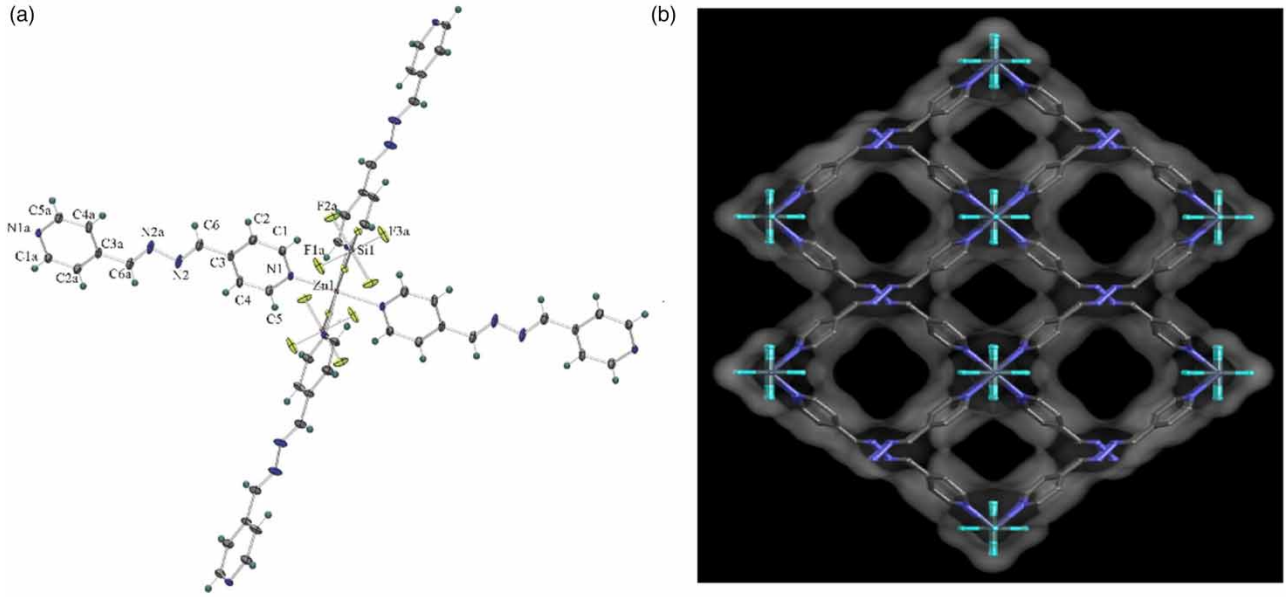

Figure 1 | The architecture of Zn-MOF reproduced from (Manna *et al.* 2018).

spacing between Zn(II) and axial F atoms being 2.153. Anions of SiF_6^{2-} have been discovered to form a link between two metal centers. The spaces of a produced metal-organic framework (Figure 1(b)) are packed with dichloromethane solution, in which the H6 atom interacts with the F3 atom at the metal node by hydrogen bonding.

According to Hou *et al.*, ZnMOF-74 demonstrated good fluorescence stability and established a hexagonal structure when Zn^{2+} had been coordinated with the carboxyl and hydroxyl groups of DOBDC linkers. ZnMOF-74, which has mean distances of 300 and 300 nanometer in the large and small axis, has excellent dispersion in aqueous electrolyte and provides superior day-to-day stability, making it an attractive fluorescent sensing system for Fe^{3+} diagnosis in a source water. Dang *et al.* prepared a innovate Zn-MOFs composite, [Zn(L1)(L2)] [4, 4′-bibenzoic acid-2, 2′-sulfone (L1) and 4, 4′-azopyridine (L2)]. 4 carboxylic oxygen ions from 3 L1 linkers and two nitrogen molecules from two similar L2 linkers seemed to be six-coordinated at the Zn (II) site in a novel Zn-MOF. In order to connect 3 zinc molecules, the 2 carboxylic acid factions of the L1 linker were then coordinated by two separate coordination methods, complexing coordination and monotone coordination establish. The azo connections in organic linker L2 were steady trans combinations. Zn1-N4 = 2.194 (3), Zn1-O4 = 2.169 (2), Zn1-O5 = 2.357 (3), Zn1-O3 = 2.06 (2), Zn1-O6 = 2.070 (2), and Zn1-N1 = 2.112 (3) were the bond widths (Figure 1(a)). L1 and L2 were able to span adjoining Zn…Zn ranges of 13.224 and 5.068, respectively. Curiously, there was a clear π···π stacking contact between the contrasting L1 linkers (3.51). Consequently, a three-dimensional (3D) structure was created as a result of the coordination method of Zn^{2+} atoms and the concentration influence (Figure 2) (Dang *et al.* 2020).

Li *et al.* prepared successfully MOF5. Zinc serves as the main metal in MOF5, and H_2BDC serves as the organic linker. Initially, the secondary structural component $Zn_4O(BDC)_3$ is formed by combining 4 zinc molecules and one oxygen molecule from H2BDC; Metal ions are encased within this 2nd structural component, which has an octahedron shape and serves as the frame domains. The powerful interaction force makes the entire structural system extra steady, and $Zn_4O(BDC)_3$ joins with the linker to create a three-dimensional skeletal structure with small pores. (Li *et al.* 2021b).

3. SYNTHESIS OF ZN-MOFS AND THEIR COMPOSITE

3.1. Hydrothermal method

The word hydrothermal comes from a geology term. Sir Roderick Murchison (1792–1871), a British geologist, used the word to explain how water at high temperatures and pressure causes changes in the earth's crust, resulting in the production of numerous rocks and minerals (Byrappa & Yoshimura 2012). In general, the hydrothermal process involves the use of a

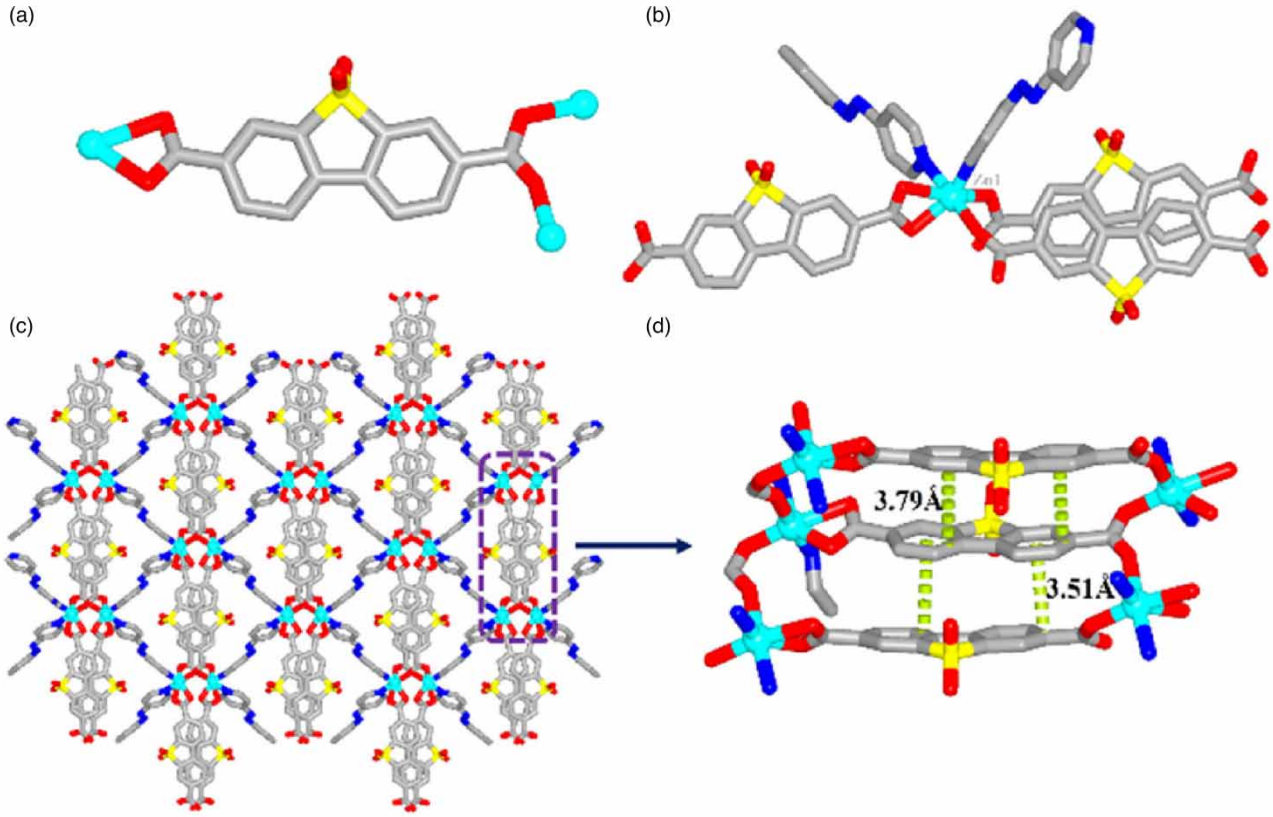

Figure 2 | X-ray formation of 1's single crystal. L1's linker coordination shape (a); Zn^{2+} ionic species' atmosphere for coordination in 1 (b observe of the first's 3-dimensional structure (c); observe of the π···π stacking interaction (3.79 and 3.51) among the L1 linkers (d) reproduced from (Dang *et al.* 2022).

high-temperature, high-pressure aqueous solution to permit the dissolution and recrystallization of otherwise insoluble material (Wang *et al.* 2022c). It has been widely used in material synthesis, chemical reactions, and waste-material treatment, and has evolved into a vibrant field of scientific investigation (Erwei *et al.* 1996).

Hydrothermal techniques were used to make a variety of MOFs with various sizes, morphologies, and crystalline structures. Even though numerous MOFs have been described to date, there are still various obstacles that remain before they may be employed in many functions, such as surface charge, size, shape, toxicity, and stability. These characteristics are not distinct and interact with one another (Chen & Wu 2018).

Dang *et al.* (2014) developed a new 3-dimensional acylamide MOF, namely Zn(L) (BPDC)·H_2O(1, $BPDC^2$ = biphenyl-4,4′-dicarboxylate,L = N,N′-diphenyl-terephthalamide) by solvo(hydro)thermal process. solid-state luminescence, thermogravimetry, and Single-crystal X-ray diffraction studies were used to describe this polymer.

Hajiashrafi & Kazemi (2019) produced ZnO nanoparticles using a simple and reproducible process involving thermal decomposition of a zinc-based metal-organic framework (Zn-MOFs). The self-assembly of dehydrating benzene-1,4-dicarboxylate (BDC) as metal ion sites and organic bridging ligands and zinc acetate, led to the creation of MOF-5 in dimethylformamide (DMF) as a solvent in the present and absent tri-ethylamine (TEA) as capping agent. FTIR was used to investigate functional groups, XRD was used to determine the crystalline structure, SEM was used to evaluate size and morphology, EDS to look into chemical properties, and diffuse reflection spectroscopy (DRS) was used to investigate UV protective properties.

Zhao *et al.* (2018a) used a hydrothermal technique to make Zn_2GeO_4/Mg-MOF-74 composites. The TEM images, SEM images, and XRD patterns show that the Zn_2GeO_4/Mg-MOF-74 composites were successfully synthesized. The close connection between Zn_2GeO_4 and Mg-MOF-74 is ascribed to tetramethylammonium hydroxide (TMAOH) coated on Zn_2GeO_4 interacting with the MOF-74's Mg-2,5-dioxide-1,4-benzenedicarboxylate (H_4DOBDC), founded by IR spectrum and TEM images.

Wei *et al.* (2020) synthesized Zn-MOFs by a hydrothermal method. In their work, Zn^{2+} and 5,10,15,20-tetrakis(4-carboxyphenyl)porphyrin (TCPP) were integrated into a porphyrin paddlewheel framework (Zn-MOF). Studies have shown that the electrochemiluminescence property of the produced Zn-MOFs material has been enhanced after it was composited with graphene oxide (GO).

3.2. Coprecipitation method

Solutions-based approaches, particularly coprecipitation, which has been used for some time and developed in the early twenty-first century, are one of the most significant methods for synthesis. Coprecipitation is the most simple, suitable, and efficient approach (Laurent *et al.* 2008). The three main steps of saturation, nucleation, and growth determine the shape of the synthesized material. The salts employed, the pH of the solution, the temperature, and the ionic strength of the media all influence the size, shape, and composition of the produced particles (Roostaee & Sheikhshoaie 2020).

There are two steps in the coprecipitation process: the first happens when the species concentration approaches supercritical saturation and tiny nuclei are created. In the next step, the growth of the crystal occurs due to the diffusion of the solutes to the surface of the crystal (Roostaee & Sheikhshoaie 2020).

The fundamental advantage of using this technique is that it produces a large number of nanoparticles, however, particle size distribution control is limited since the kinetic agent is regulated by crystal growth (Dong & Koenig 2020). Currently, many metal-organic frameworks are prepared using the co-precipitation method.

Wang *et al.* (2018b) used a simple co-precipitation approach to successfully synthesize a hierarchical and hollow MOF composed of parallel stacked triangular sub-MOFs. The hollow MOFs were then transformed into composites made of binary metallic nanoparticles and carbon, such as Zn–Mn mixed oxides@carbon (ZnxMnO@C). The resulting ZnxMnO@C retains the MOF precursor's particular hollow hexagonal nanodisks (HHNDs) structure, and each triangular plate-like component is made up of a continuous carbon matrix inserted evenly inside the nanoscale ZnxMnO nanostructure.

Liang *et al.* (2020) synthesized MOF-derived spinel $ZnCo_2O_4$/ZnO/C heterostructure anode. Using two-step annealing of cyanide-bridged coordination polymer initial compounds, spinel $ZnCo_2O_4$/ZnO/C hierarchically nanostructured materials were effectively produced. The regular cube structure and a high surface area, enhance charge transfer into the electrode materials and provide good charge transport kinetics, as shown by hierarchically porous compounds.

Opelt *et al.* (2008) successfully used a coprecipitation technique to manufacture 0.5 wt. percent palladium supported on MOF-5. The observed surface area reached around 900 m^2/g, the effective micropore size was approximately 0.3 cm^3/g, and the powder X-ray diffraction patterns matched the predicted pattern of MOF-5 well. MOF-5 is a common MOF composed of benzene-1,4-dicarboxylate as linkers producing a cubic network and $Zn_4O_6^+$ clusters as metal centers.

3.3. Sol-gel method

Sol-gel preparation is an efficient and flexible approach for the fabrication of functional inorganic and hybrid compounds that allow for molecular composition control as well as material organization at various length scales important to basic and practical research (Ghazal *et al.* 2021). Recent advancements have made it possible to utilize it to manufacture MOFs (Park *et al.* 2016). Sol-gel techniques can be used to manipulate MOFs directly or as a pathway to the creation of composite materials in which the MOF's characteristics are synergistically mixed with those of a properly chosen inorganic component. In this study, we highlight the most notable advances in this growing field, organized around four primary synthetic techniques, with a special emphasis on demonstrating how sol-gel processing improves the capabilities of the MOF. These strategies include: (1): MOF crystals are controllably positioned or grown on inorganic surfaces (2): sol-gel precursors were used to manipulating the pore surfaces of MOFs on a molecular scale (3): the utilization of sacrificial inorganic templates produced from sol-gel for the creation of MOF-based architectures and (4): the employment of MOF crystals as sol-gel process templates (either within the pores or at the external surfaces) (Au *et al.* 2016). Every one of those processing techniques gives distinct features to the systems and provides a path to higher-order structures and material compositions not available by traditional MOF synthesis processes. The sol-gel method offers prospective paths toward novel functional compounds with increased features, and it is expected to play a significant role in enabling MOFs to be optimized for various applications (Sumida *et al.* 2017).

Alwin *et al.* (2018) synthesized TiO_2 aerogel–Zn-MOFs nanocomposite using the sol-gel technique. With the help of glacial acetic acid and deionized water, titanium isopropoxide (TIP) was fixed. For 1 hour, the titania sol was rapidly stirred. In the titania sol, around 10% Zn–MOFs for TIP were added, and the solution was stirred for 2 hours. The reported approach was used to make the MOF [Zn(N-(4-pyridylmethyl)-L-valine·HCl)(Cl)]$(H_2O)_2$. The BET result shows surface area of the

nanocomposite material which was 250 m^2g^{-1}, with an average pore size of 5 nm. The continuous organization of the pore-solid network structure was shown by field emission scanning electron microscopy (FESEM) images. The existence of MOF clusters on the TiO_2 aerogel network is shown by energy-dispersive X-ray analysis. The presence of specific oxygen vacancies in the nanocomposite material is further confirmed by an X-ray photoelectron spectroscopic study, which also supports the formation of MOF clusters in the aerogel system.

3.4. Sonochemical method

Sonochemistry is the study field of molecules that undergo chemical reactions as a result of the application of strong ultrasonic radiation (20 kHz–10 MHz). Acoustic cavitation is the physical phenomenon responsible for the sonochemical method. Sonochemical approaches based on homogenous and rapid nucleation can also produce a shorter crystallization time and also much smaller particle size than the traditional solvothermal approach. The sonochemical approach is a simple, effective, and extensively used strategy for the preparation of MOFs. A base solvent combination for one certain MOF structure is injected into a horn-type pyrex reactor fitted with a sonicator bar with an adjustable power output that does not require external cooling Acoustic produced cavitation occurs when bubbles in a solution following sonication develop and collapse, resulting in extremely relative high temperatures (5,000 K) and pressures (1,000 bar), (Sonbol *et al.* 2021b; Moghadam *et al.* 2022), as well as incredibly rapid heating and cooling speeds (>1,010 K/s) that produce ultrafine crystallites. In 24 hours at ambient temperature, Wiwasuku *et al.* employed sodium acetate as a modifying agent and ultrasonic irradiation to produce homogeneous Zn-MOFs octahedral microscopic particles with a mean range of 1.7 μm. The microparticles obtained from the ultrasonic approach have a higher detection sensitivity than the polycrystalline Zn-MOFs because of their smaller size. The two uncoordinated Lewis basic sites have a big impact on the detection's sensitivity and selectivity (Wiwasuku *et al.* 2020).

For the first time, Son *et al.* (2008) used a sonochemical technique to generate extremely good quality MOF-5 crystals of 5–25 μm in size in a substantially shorter synthesis time (ca. 30 min) than the traditional synthesis process (24 h).

Abuzalat *et al.* (2018) in this research used sonochemical processes to establish a quick and simple approach for creating metal-organic framework films *in situ* on zinc or copper metal substrates. The precursor was initially treated with a powerful oxidant to convert the metal to the appropriate metal hydroxide. Ultrasonic (Guan *et al.* 2021) irradiation provided sufficient energy to initiate the reaction between organic linkers and metal ionic species. This method was used to successfully synthesize 4 MOF films (Cu-BDC, Cu-BTC, MOF-5, and ZIF-8). Characterization of the films was done using SEM and XRD analysis. The influences of ultrasonic irradiation duration and organic ligand concentration on the production of MOF films were also thoroughly explored. The quick and simple manufacturing process described in this research might lead the way for the growth of MOF films on diverse gas sensor surfaces.

Abdollahi *et al.* (2018) produced a 3-D Zn(II)-based MOF of $[Zn_4(oba)_3(DMF)_2]$ by sonochemical and solvothermal techniques employing the nonlinear dicarboxylate ligand, 4,4′-oxybis(benzoic acid) (H_2oba). The influence of various irradiation durations and concentrations of primary reagents on the achievement of monotonous morphology was explored. The results suggest that extending the duration of irradiation and reducing the concentration can result produce homogenous nanoplates. The influence of the synthesis process on the porosity of the framework was investigated using N_2 adsorption.

3.5. Polyol method

After almost several decades of research, the polyol technique is now commonly recognized and employed as a unique flexible chemical technology for the manufacture of a wide range of nanoparticles that may be used in significant technical areas. This approach has several advantages, including the convenience of use, low cost, and, most significantly, scalability for industrial uses. Metals were the first category of inorganic nanoparticles to be described as being able to be produced in liquid polyols. This method's ability is also demonstrated in the fabrication of alloys, inter-metallic, core-shell nanostructures, and MOFs with a wide range of compositions (Fiévet *et al.* 2018).

Khan *et al.* (2014) developed carbon with porosity (PC-900) by rapid carbonization of porosity MOF-5 ($Zn_4O(bdc)_3$, bdc = 1,4-benzenedicarboxylate) at 900 °C. Using the polyol reduction process, the carbon substrate was covered with PtM (M = Ni, Fe, Cu, and Co (20% metal concentration) nanostructures, and the catalyst PtM/PC-900 was produced for fuel cells (DEFCs). The XRD, and EDS techniques were used to characterize this catalyst.

3.6. Electrochemical method

Under oxidizing conditions, the electrochemical technique may be utilized to produce metal-organic frameworks. Electrons are used as reactants in this technique. It is a non-polluting procedure that does not pollute the environment. However, platinum, which is employed as an electrode, is expensive (Roostaee & Sheikhshoaie 2020).

The mixed-ligand Zn-based MOF [$Zn(1,3\text{-bdc})_{0.5}$(bzim)] was synthesized by de Lima Neto *et al.* (2019) by using an electrochemical technique. In studies of various process parameters, the current density and duration of reaction were shown to be the most important factors impacting the purity and yield of the result. A 120 minutes reaction duration and A 60 mA current were determined to be the optimal conditions for obtaining pure-phase MOF with maximum yields (87%). When compared to traditional diffusion, hydrothermal, and solvothermal procedures, the applied synthesis conditions enabled a considerable reduction in response time and crystallite size. FT-IR, PXRD, thermogravimetry (TG), BET, and SEM were all used to properly describe the most promising sample.

4. CHARACTERIZATION OF ZN-MOFS

The synthesized Zn-MOFs can be characterized with several instruments and methods. Numerous sciences, including pharmacology, physics, mathematics, statistics, and medicine, have advanced considerably in recent decades (Hajiseyedazizi *et al.* 2021; Rashid *et al.* 2021; Zhao *et al.* 2021e; 2021f; Jin *et al.* 2022; Rashid *et al.* 2022b; Wang *et al.* 2022d). Characterization methods are one of the most important advances in science. The morphology of Zn-MOFs composites was investigated by SEM and TEM images. The purity of synthetic compounds can also be obtained by EDS analysis. One of the most important methods for characterizing Zn-MOFs is XRD, which presents the crystal structure of the synthesized compound. BET and FT-IR are other methods of characterizing Zn-MOFs, which are described below characterization of Zn-MOFs composites with these methods.

4.1. XRD patterns of Zn-MOFs

XRD methods were used to further analyze the crystal structure of Zn-MOFs-1. Based on single-crystal XRD data, Zn-MOFs-1 is constructed using $Zn_2(-COO)_4(\text{-}Py)_2$ pillared paddlewheels as supplementary building components (SBUs), that have 6 coordinates coupled by $BPDC^{2-}$ and DPyF, the SBU ligates 2 Zn (II) ions with 4 O atoms from carboxylate groups and one pyridine N atom, leading in deformed tetrahedral structures. Each SBU subsequently connects four neighboring SBUs with $BPDC^{2-}$ ligands to form 2D layer structures that are supported by a pyridine-based DPyF linker to form 3D frameworks (Wang *et al.* 2021b).

Ling *et al.* (2019) used PXRD to confirm the structural properties of Cu–ZnMOF. Peaks were assigned to the (100), (110), and (004) planes at 5.82°, 7.49°, and 13.80° indicating the sheet structure and effective assembly of Cu–ZnMOF.

Li (2021) recorded the PXRD pattern Zn-MOFs. Figure 3 depicts the XRD of a synthesized ZnMOF, indicating that this metal-organic framework was successfully produced.

Hou *et al.* (2019) demonstrated in their study that the XRD pattern of synthesized Zn-MOF-74 corresponded well with that of simulated Zn-MOF-74. Zn-MOF-74's characteristic diffraction peaks emerged at $2 = 6.8°$ and $2 = 11.7°$, which were associated to the (110) and (300) facet, respectively (Mjejri *et al.* 2017). According to the given characterization data, high crystalline Zn-MOF-74 was successfully fabricated.

Bagheri *et al.* (Schweighauser *et al.* 2017) investigated the crystalline characteristics of the as-synthesized composites using the XRD technique. The major peaks in the diffraction pattern of flake-like MOF were obtained at 2θ values of approximately 10.7, 11.6, 12.7, 17.5, and 25.1° (Bagheri *et al.* 2018). Schweighauser *et al.* reported comparable diffraction peaks for Zn-TA 2D MOFs.

4.2. SEM and EDS images of Zn-MOFs

SEM images are important for microscopy for the characterization of the material (Liu *et al.* 2021c, 2021d; Jasim *et al.* 2022c). Zhang *et al.* (2020) created the Zn-MOFs (MOF-5) and Ni@MOF5. Figure 4 represents the microstructures and typical morphologies of samples. SEM images of MOF-5 and Ni@MOF-5 materials are shown in Figures 4(a) and 4(b). Figure 5(a) shows that the size of the MOF-5 (2 μm) used in this study is significantly smaller than the size of the cube MOF-5 (20–200 μm) described in the studies, demonstrating that the size of the crystal may be decreased under continuous stirring circumstances.

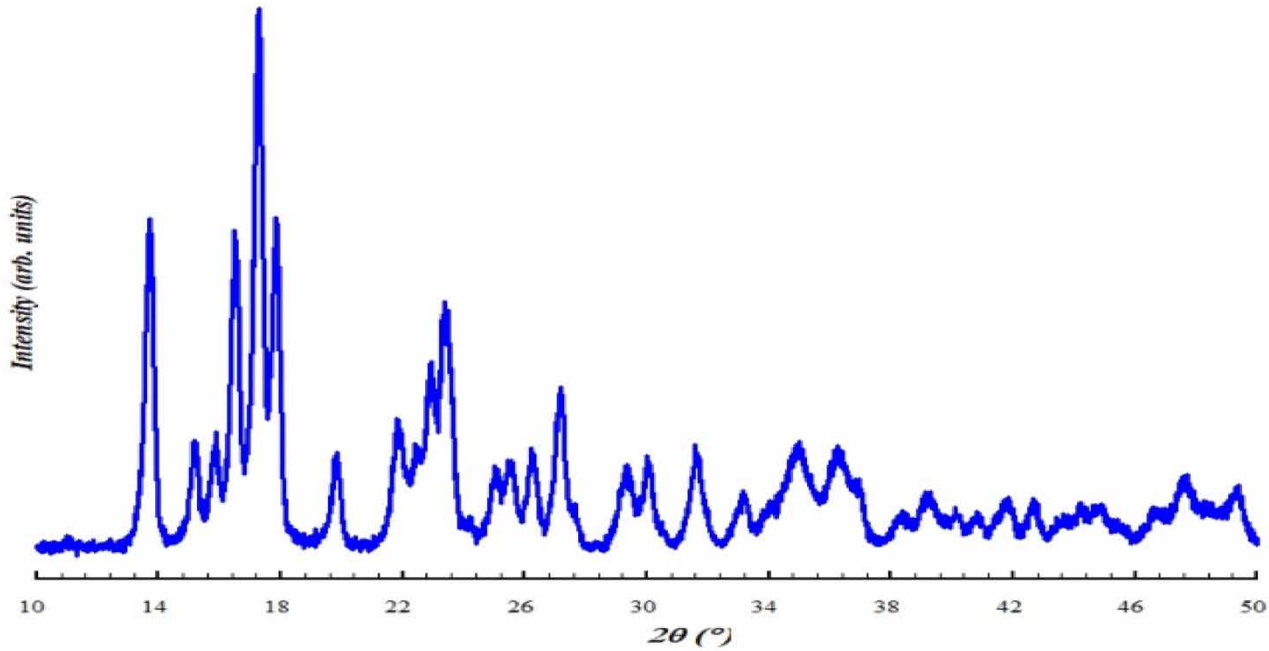

Figure 3 | XRD pattern of Zn-MOFs reproduced from (Li 2021).

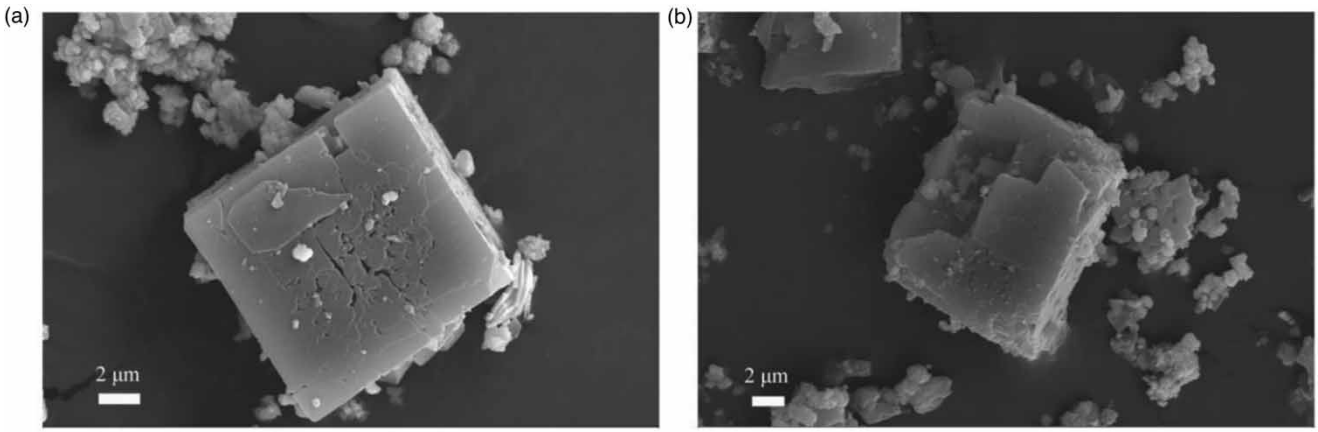

Figure 4 | SEM images of (a) MOF-5 and (b) Ni@MOF-5, reproduced from (Zhang *et al.* 2020).

Figure 4(b) shows SEM images of 5 percent Ni@MOF-5. The SEM image of the 5 percent Ni@MOF-5 compound is not considerably dissimilar from the structure of MOF-5, demonstrating that the adding of Ni^{2+} does not affect the original crystal's morphology.

Moradi *et al.* (2019) prepared successfully MOFs known as $Zn_2(oba)_2bpy$, (1; H_2oba = 4,4-oxybisbenzoic acid and bpy = 4,4-bipyridine) linkers. Figure 5 illustrates SEM images of a produced MOF.The sizes and morphology of synthesized nanostructures are affected by a variety of factors, including the concentration of the initial reactants (Kim *et al.* 2011). To study the influence of this factor on the size and morphology of the MOF, SEM was used to characterize the sample produced using a varied concentration of initial chemicals. Figure 6 illustrates SEM images of MOF produced at various initial reactant concentrations of 0.01, 0.02, and 0.04 M. Increased levels of the preliminary chemicals reduced crystallite diameter, as shown by the compared of specimens of different doses (Figure 6(c) and 6(d)).

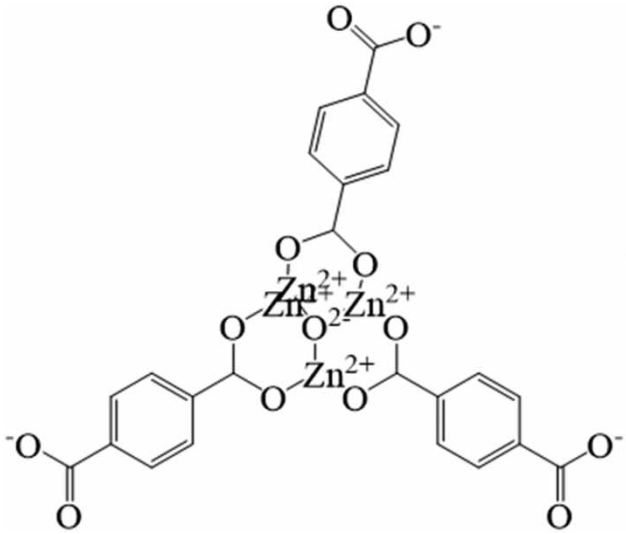

Figure 5 | Schematic diagram of chemical structures for MOF5 reproduced from (Li *et al.* 2021b).

Patel *et al.* (2018) successfully synthesized amine-functionalized Zn(II) MOF. The crystalline material for produced MOF has a well-defined shape, as shown in SEM images of this composite.

Ling *et al.* (2021) prepared MOF sheets (Zn–ZnMOF) with Zn as the node and zinc(II)tetraphenylporphyrin (TCPP(Zn)) as the linker. Initially, SEM images was used to investigate the morphology and size of the generated Zn–ZnMOF sheets. The result indicated that the Zn–ZnMOF could be characterized by SEM images that have a sheet-like shape with a diameter of hundred nanometers, indicating that the Zn–ZnMOF sheets are ultrathin. The existence of carbon, nitrogen, oxygen, and zinc elements in the Zn–ZnMOF was also shown by energy-dispersive spectroscopy and SEM elemental mapping.

Rosales-Vázquez *et al.* (2020) invented by reacting Zn(II) ions in DMF with 1,4-benzenedicarboxylic acid (H_2BDC) and isoquinoline (iQ), a new blue photoluminescent 2D MOF with the composition $[Zn_2(2\text{-}BDC)2(iQ)_2]$ was generated with good solvothermal performance. SEM and EDS analysis were used to investigate the crystalline substance. According to images taken using a scanning electron microscope, there are micrometric bands with a well-defined plane pointing in the transverse direction. The SEM images show the edge of a bar with the expected cleavage for monoclinic crystals, confirming the crystal system discovered by XRD research. The results demonstrate that the morphology is homogeneous, which may be due to the existence of only one phase in the monoclinic unit cell. EDS elemental mapping of Zn-MOFs is also investigated. EDS analysis shows the existence of C, O, and N in the sample's chemical composition; additionally, the signal of Zn atoms was identified throughout the crystals, indicating a homogenous distribution of Zn in the produced compound.

4.3. TEM images of Zn-MOFs

Rani & Kataria (2021) report a highly effective synthesized zinc–metal-organic framework-8 and silver quantum dot (Zn-MOF-8@AgQDs) composite. TEM image was used to investigate the size and morphology of the metal complex and its composite. TEM pictures of Zn–MOF-8 nanostructures and their QDs composites are shown in Figure 7. Figure 7(b) exhibits the Zn–MOF-8 exhibited cube-shaped morphologies with sizes ranging from around 186 nanometers. Furthermore, the Zn-MOF–8@Ag composite demonstrated that Ag particles adhered to the surface of the Zn–MOF-8. Figure 7(c) shows that Ag QDs particles have a strong attachment to the surface of Zn–MOF-8, leading to a smooth route for electron collection and transmission.

Compound adsorption substances combine the benefits of a variety of adsorptive chemicals while also compensating for the shortcomings of individual adsorbent materials. The adsorption characteristics of magnetic montmorillonite (MMMT) for Pb are excellent (II). Shen *et al.* Zn-BDC, a type of MOF, was produced and *in situ* polymerized onto the surface of MMMT to improve the material's adsorption properties. TEM images were used to characterize the composite material MMMT@Zn-BDC. The composition and internal structures of Zn-BDC, MMMT, and MMMT@Zn-BDC were studied using TEM. According to the results, the Fe_3O_4 nanoparticles are roughly uniform, whereas the irregular crystals are

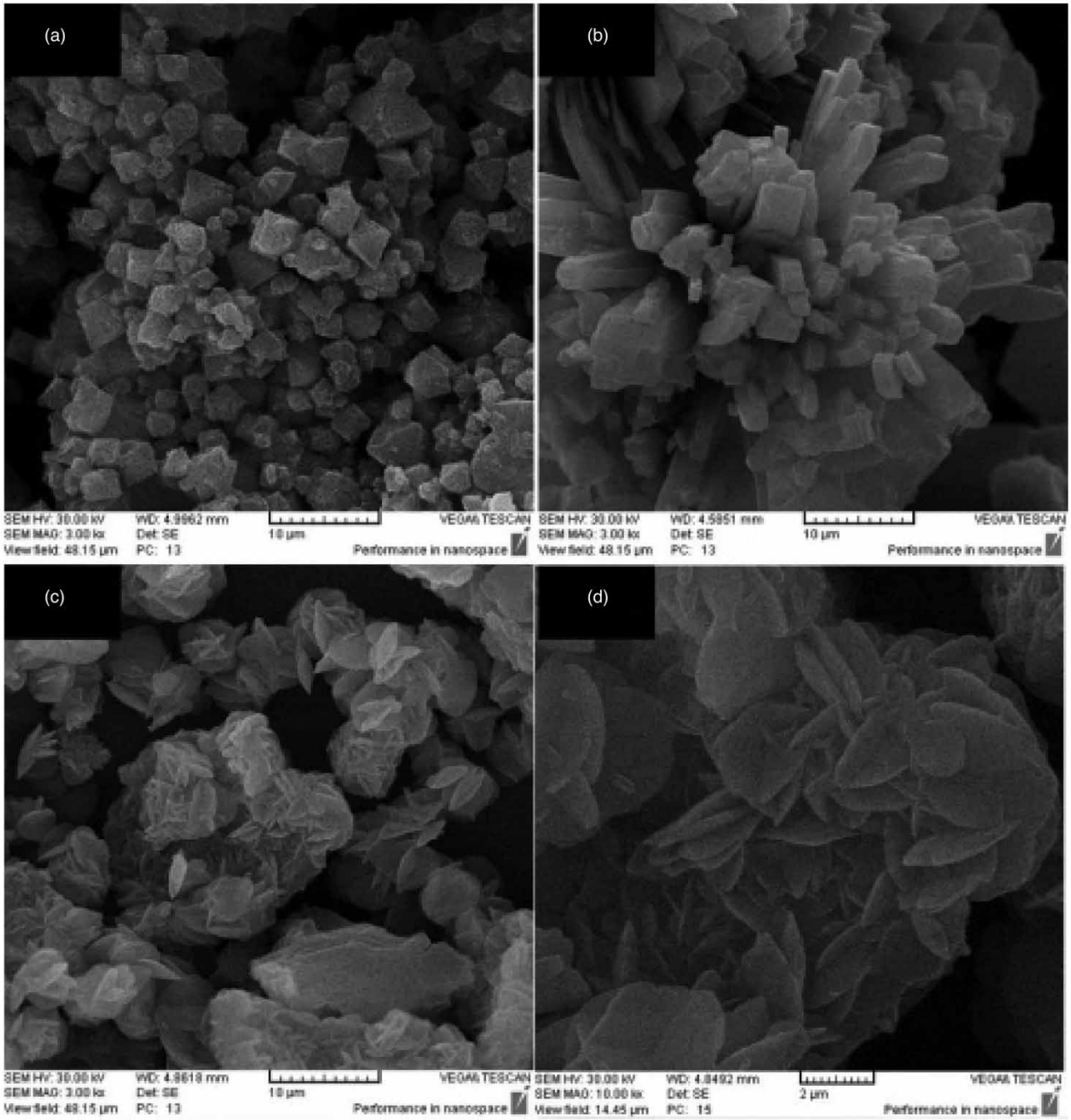

Figure 6 | SEM images of $Zn_2(oba)_2(bpy)$ nanostructures generated in varied concentrations of starting chemicals after a 1 h irradiation time: (a, b, and c, d) 0.01 M, 0.02 M, and 0.04 M, reproduced from (Moradi *et al.* 2019).

MMT. On the same surface, Fe_3O_4 and MMT are nearly evenly distributed. The successful preparation of MMMT was approved. According to TEM images, the Zn-BDC crystals are generally irregular and have a narrow lattice structure. A thin lattice structure emerged after preparing Zn-BDC on the MMMT area. Finally, it was determined that a thin lamellar structure had been effectively produced (Shen *et al.* 2018).

Hu *et al.* (2018) created an electrochemiluminescence (ECL) sensor for the detection of clenbuterol using a unique zinc-based metal-organic framework–reduced graphene oxide–CdTe quantum dots (ZnMOF-RGO-CdTe QDs) hybrid. The morphology of the prepared nanostructures was investigated using TEM. The results reveal that the CdTe QDs were

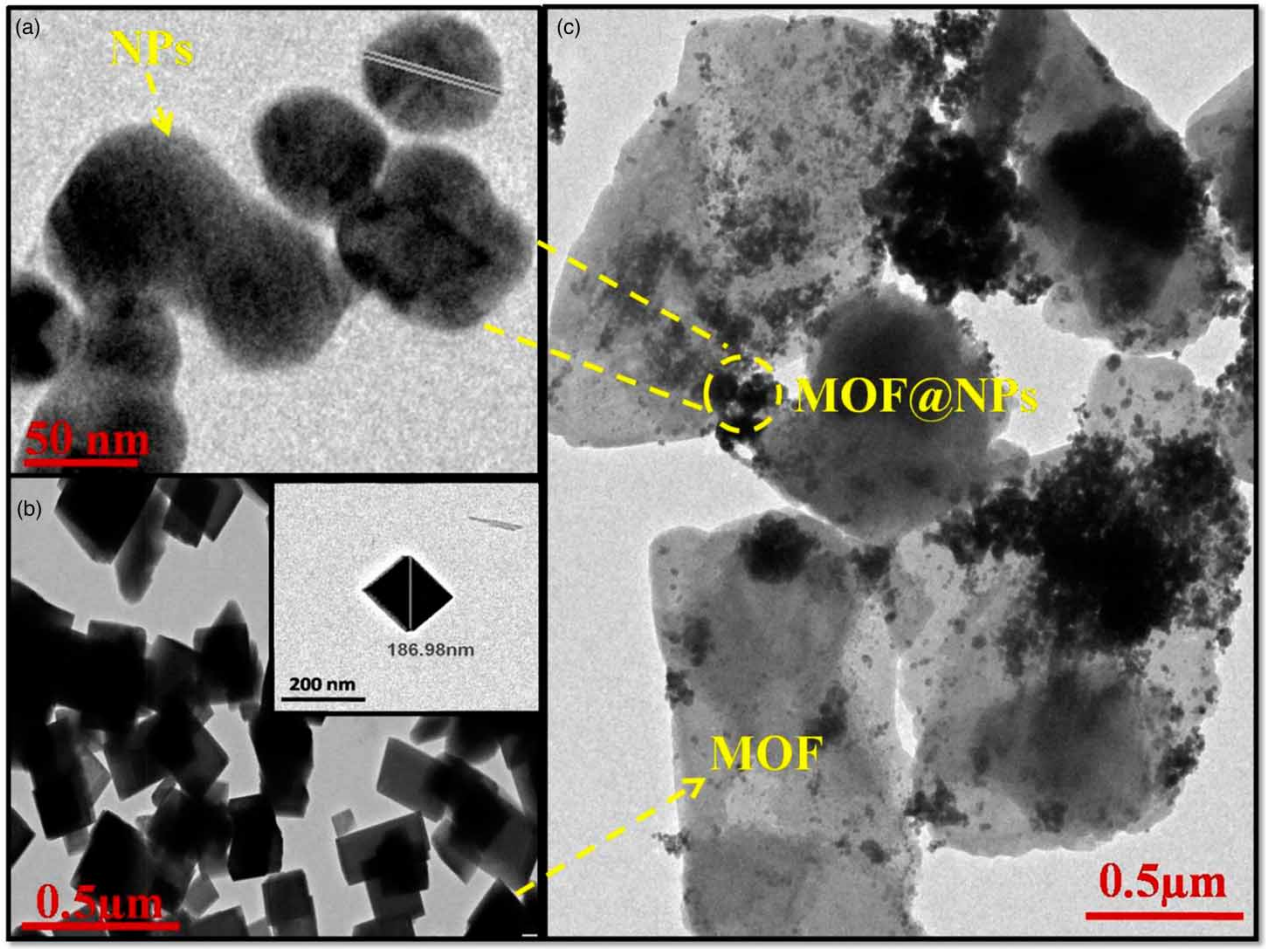

Figure 7 | TEM image of (a) Ag QDs particles, (b) Zn–MOF-8, (c) Zn–MOF-8@AgQDs, reproduced from (Rani & Kataria 2021).

distributed evenly on the RGO substrate. It was also possible to determine the particle size distribution. The CdTe QDs had an average particle size of 3.8 ± 0.5 nm, which was comparable with prior results (Yu *et al.* 2016). The TEM images of the ZnMOF-RGO-CdTe QDs clearly illustrate the formation of the RGO-CdTe QDs and Zn-MOFs structures. The Zn-MOFs without RGO-CdTe QDs had an average particle size of 0.34 ± 0.02 μm, which was comparable with earlier research (Stock & Biswas 2012). The presence of RGO affects the development of Zn-MOFs, as evidenced by images of Zn-MOFs and ZnMOF-RGO-CdTe QDs. In the presence of RGO, the particle size of the Zn-MOFs reduced, and their surfaces became rough.

4.4. BET of Zn-MOFs

Ribeiro *et al.* (2021) synthesized Zn(dcpa) MOF (dcpa (2,6-dichlorophenylacetate). At 77 K, N_2 adsorption was used to measure the porosity of Zn(dcpa). Figure 8 illustrates the resulting isotherm, which indicates a starting stage continued by a gradual increase to $p/p_0 = 0.06$; after that, there is another significant rise until approaching a virtually constant plateau with just a little increase between $p/p_0 = 0.2$ (274 cm^3/g) and $p/p_0 = 0.97$ (303 cm^3/g). At 77 K, p and p_0 are the adsorbate's equilibrium and saturation pressures, respectively. Liu *et al.* (2013) reported a similar response, attributing the first phase of the isotherm to the Zn(dcpa) composition with shrinking porosity and the second phase to an extended structure. The extended structure in this study had a particular pore size of 0.47 cm^3/g, computed at a relative pressure of $p/p_0 = 0.97$, assuming the holes were packed with fluid N_2 at their normal boiling point. one desorption branch displayed hysteresis at $p/p_0 = 0.2$, which is consistent with a prior study, however in this example, the hysteresis loop looked to shut at lower pressures, indicating a recovery to the shrunken pore form, contrary to Liu *et al.* finding.

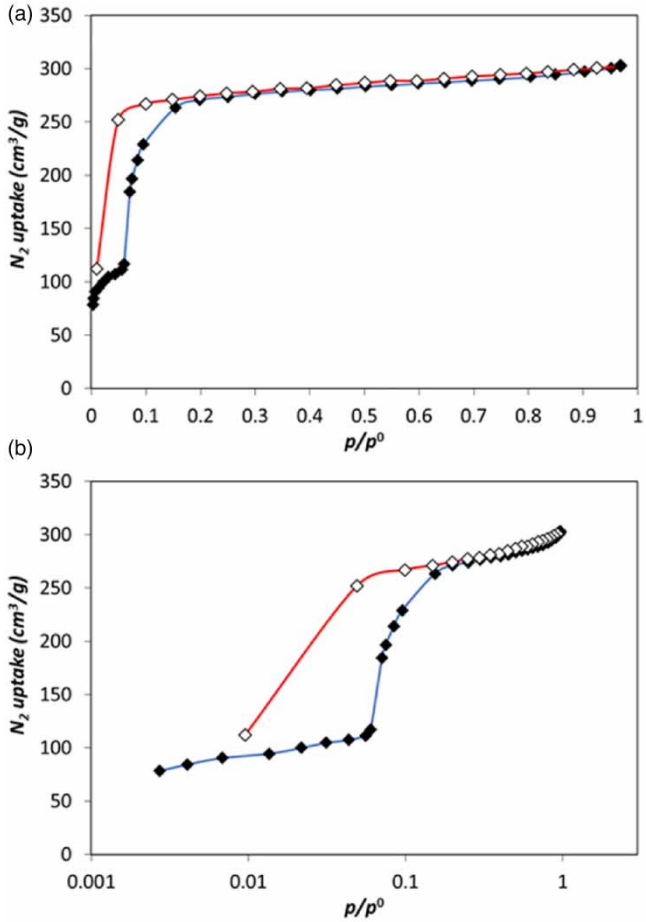

Figure 8 | At 77 K, the N_2 adsorption equilibrium isotherm on Zn(dcpa) in linear (a) and log (b) scales. The adsorption and desorption data are represented by filled and empty symbols, respectively, reproduced from (Ribeiro *et al.* 2021).

Li *et al.* (2019) used a metal-organic framework with high stability, namely $((ZnCl_2)_3(L)_2DMF)_n$, where L = 1,3,5-tris((pyridin-4-ylthio)methyl)benzene(MOF 1), to degrade or adsorb tetracycline from wastewater. The findings indicate that MOF 1 performed well in the adsorption of tetracycline. The BET technique was used to determine the adsorption properties of the manufactured adsorbents. The hysteresis of the data obtained from MOF 1 was type-H3, and the adsorption-desorption isotherm curve was compatible with the usual type-IV isotherm, as predicted by the volume filling theory of mesoporous. The pore size and total surface area of MOF 1 were 4.7 and 11.86 nm, respectively, according to the BET and DFT techniques (Li *et al.* 2020).

4.5. FT-IR spectra of Zn-MOFs

Yang *et al.* (Zebardast *et al.* 2018) used a simple solvothermal approach to create MOF-5 and bimetallic MOF-5 (Co/Zn and Ni/Zn). Various methods, such as FT-IR, were used to characterize the samples (Figure 9). Significant bands in the IR of the parent compound at 1,578 and 1,381 cm^{-1} were ascribed to asymmetric and symmetric stretching of the complexes formed of the BDC linkers, respectively (Sabouni *et al.* 2010). The in-plane and out-of-plane stretching of the aromatic C-H groups of the benzene ring found in the BDC linker is attributable to numerous small bands in the area of 1,146–1,017 cm^{-1} and 820–600 cm^{-1}, respectively. The adsorbed moisture content is shown by the bands at 3,200–3,500 cm^{-1} (Sabet *et al.* 2016). The IR spectrum of metal-doped specimens (Co/Zn and Ni/ZnMOF-5) seem to be comparable to those of one's caregiver (Pure MOF-5), indicating that the pure MOF-5 framework is preserved throughout modification, as predicted by the research (Yang *et al.* 2014).

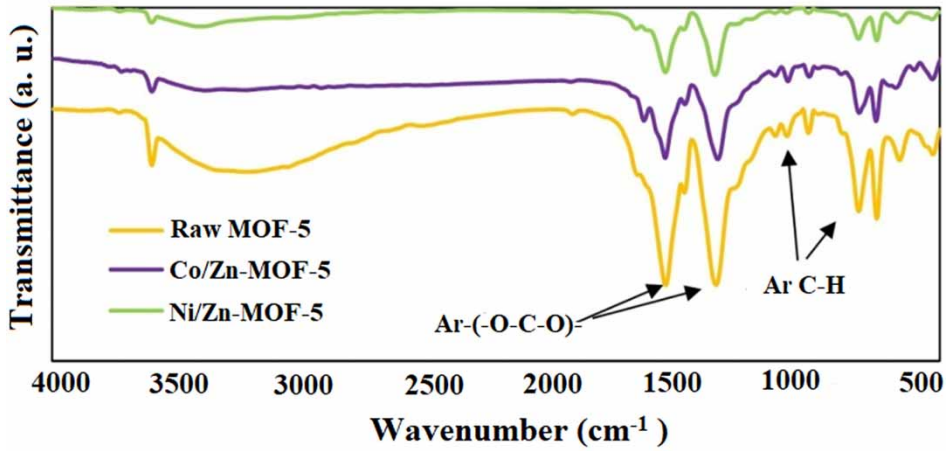

Figure 9 | As-prepared Co/Zn, Ni/Zn, and pure MOF-5 FT-IR spectroscopy, reproduced from (Zebardast *et al.* 2018).

The development of heterogeneous photocatalysis (Ma *et al.* 2022) with numerous binding sites for the production of cyclic carbonate using CO_2 and epoxide has piqued researchers' curiosity for a long time. By combining multiple functionalized ligands onto a single framework, Kurisingal *et al.* created zinc metal-based multi-variate MOFs. The FT-IR spectra further confirm that all of the catalysts are formed from their linker units and metal precursors. The O single bond H stretching frequency of coordinated water and single bond OH functionality in MOF-5 and MOF-5-OH, respectively, correspond to the wide peaks in the region of 3,400–3,450 cm^{-1}. Furthermore, the N single bond H stretching vibrations of NH_2 functionality in MOF-5-NH_2 are attributed to the two bands at 3,200–3,600 cm^{-1}. The single bond OH peak at 3,475 cm^{-1} in MOF-5-MIX may overlap the single bondNH_2 functional group peak. The C single bond H stretching vibrations are ascribed to the bands about 2,950 cm^{-1} in all catalysts. The symmetric and asymmetric stretching vibrations of the carboxylic (Cdouble bondO) functionality of the ligand are seen at around 1,675 and 1,500 cm^{-1}, respectively. The conjugated C double bond C stretching vibrations are responsible for the distinctive bands at 1,610 cm^{-1}. The symmetric stretching vibration of the Zn-O bond at 520 cm^{-1} demonstrates that Zn was successfully coordinated with the ligands (Kurisingal *et al.* 2020).

5. APPLICATION OF ZN-MOFS NANOCOMPOSITES AS A PHOTOCATALYST FOR THE DEGRADATION OF WATER POLLUTANTS

As mentioned, various sciences, including chemistry, physics, mathematics, statistics, and medicine, have advanced significantly in recent years (Chu & Zhao 2016; Zhao *et al.* 2018b, 2019, 2020b, 2020c, 2021g, 2021h; Wang *et al.* 2020; Amiri *et al.* 2021b; Karthikeyan *et al.* 2021; Xu *et al.* 2022). One of the most important of these sciences is photocatalysis and the removal of pollutants from water (Uddin *et al.* 2021). Every day, natural water supplies and, the seas are contaminated as a result of increased industrialization. Large industries generate a wide range of harmful compounds, including byproducts of textile dyes, insecticides, plastics, and organic chemical wastes (Zhang *et al.* 2015; Arora *et al.* 2021). As a result, the removal of toxic sewage has become one of human society's significant issues. Huge attempts have been made to use nanomaterials as photocatalysts to degrade organic contaminants in polluted water into ecologically friendly organisms. Because of their nontoxicity, Zn-MOFs are a good semiconductor compound for this function.

5.1. Degradation of methylene blue

MB is a typical thiazine dye with the molecular formula $C_{16}H_{18}N_3ClS$ (Arora *et al.* 2019; Soni *et al.* 2020a) and is the most often used compound for coloring silk, wood, and cotton. Because of its molecular structure, it is water-soluble and chemically stable, making it one of the most widely used dyes in the industry (Huang *et al.* 2019). MB can induce eye burns, which might result in irreversible damage to human and animal eyes. It can induce a short duration of quick or hard breathing when inhaled, whereas absorption through the mouth causes excessive perspiration, burning feeling, vomiting, nausea, methemoglobinemia, and mental disorientation (Rafatullah *et al.* 2010). Conventional water treatment procedures, on the other hand, are unable to easily remove this pollutant. Because of the negative effects on receiving waterways, the treatment of receiving waters containing such dye is of importance (Xue *et al.* 2022).

Utilizing a hydrothermal strategy, Sindhu *et al.* synthesized a 3D supramolecular zinc integrated MOF by 4,4'-bipyridine as the co-ligand and 2,6-naphthalene disulphonic acid as the ligand. Various analytical methods were used to characterize the MOF for its composition, functional groups, shape, and crystal structure. The photocatalytic activity of MOF under visible illumination was investigated for the destruction of MB. The synthesized MOF was reported to be nanocrystalline and had a bandgap of 3.4 eV, according to the results. When hydrogen peroxide was added as an electron acceptor to a Zn-MOFs and dye analyte solution, the photocatalytic activity was significantly increased. Dye degradation is accomplished by ligand-to-metal charge transfer (L-MCT). The accelerated oxidation process is responsible for the increased photocatalytic performance in the existence of an acceptor of an electron. The molecules involved in photocatalytic removal of MB utilizing Zn-MOFs include hydroxyl radicals and holes, according to scavengers trapping observations. The MOF's stability is demonstrated through leaching studies. During recycling studies, the reusability of Zn-MOFs as a photocatalyst for the decomposition of dye molecules such as MB was demonstrated. Recyclability is critical for the practical application of photocatalysts. Reuse tests were performed to determine the reusability of Zn-MOF. The photodegradation process generated a final product that had been washed with ethanol and used again in the following photodegradation period. The results show that the Zn-MOF is still active since 5 period. With no discernible activity decrease for MB Photodegradation, the photocatalytic efficiency drops from 92 percent to 85 percent of MB percentage removal, demonstrating outstanding good stability. The kinetics of some processes were also analyzed (Abdelhameed *et al.* 2021b; Emam *et al.* 2021). Applying the equation $\ln (C/C_0) = kt$, where C and C0 are the content of CP at preliminary and t moment, the pseudo-first-order percentage constant k had been described to recognize the kinetic model of the MB decomposition reaction. The *Langmuir-Hinshelwood* formula was used to fit the data into a first-order model to study the reaction mechanism of the Zn-MOF photocatalytic activity. This equation shows a linear correlation among $\log(C/C_0)$ and the time (t) required to degrade MB (Sindhu *et al.* 2021).

The photodegradation efficiency of three ZnO samples was investigated following UV light irradiation every 30 minutes for 3 h in 3 experiments, as shown in Figure 10 and Table 1. The performance of ZnO photocatalysts with various ZnO cube, octahedron, and cuboctahedron, morphologies is 72.70 percent, 82.38 percent, and 85.79 percent, respectively, according

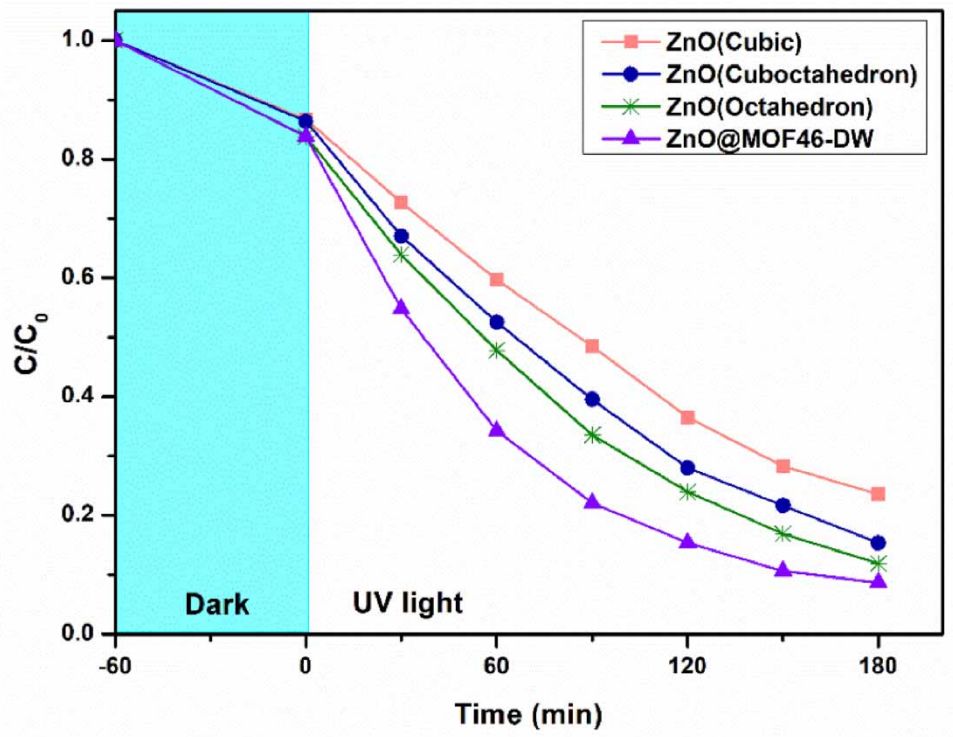

Figure 10 | Relative methylene blue concentration change at various time intervals with prepared ZnO as the photocatalyst reproduced from (Buasakun *et al.* 2021).

Table 1 | Photocatalytic efficiency of all prepared ZnO and ZnO@MOF-46(Zn)-DW, reproduced from (Buasakun *et al.* 2021)

Samples	Experiment 1	Experiment 2	Experiment 3	Average degradation (3hours)	Average degradation (1hours)
ZnO (Cube)	66.64	74.70	76.78	72.70	30.98
ZnO (Cuboctahedron)	74.25	83.36	89.52	82.38	39.35
ZnO (Octahedron)	81.83	85.38	90.16	85.79	42.92
ZnO@MOF-46(Zn)-DW	89.53	90.24	90.51	90.09	61.20

to the findings. The octahedral structure of ZnO provides the maximum ability in dye photodegradation (Buasakun *et al.* 2021). The optical properties are another explanation for photodegradation efficiency. All synthesized ZnO exhibits UV-visible spectra in the UV region, which are related to the energy for electron transition. Octahedral ZnO has the highest absorption intensity, but it is only slightly stronger than cubic ZnO. Furthermore, UV-visible spectra measurements were used to calculate the band gap energy of ZnO using the Kubelka–Munk method, as shown below.

$$(\alpha h\nu)^2 = K(h\nu - Eg)$$

where $h\nu$ is the photon energy (eV), K is a constant related to the material, α is the absorption coefficient, and Eg is the band gap energy (eV). The band gaps of cubic ZnO(1), cuboctahedral ZnO(2), and octahedral ZnO (3) are 3.28, 3.15, and 3.11 eV, respectively. Therefore, the morphologies of synthesized ZnO affect the absorption range and band gap energy. Octahedral ZnO reveals the lowest band gap energy, which is related to the highest photocatalytic efficiency.

Ye *et al.* (2016) used diffusion in an H_2O–MeOH solvent system to produce several novels MOFs consisting of a transition-metal organic acid salt and 2, 5-bis(3-pyridyl)-3,4-diaza-2,4-hexadiene (3-bpdh). The findings showed that building blocks and metal-ion potential should be used to produce MOF self-assembly. The composite photocatalyst TiO_2@Zn-MOF was created by coating MOF microcrystals with titanium dioxide and demonstrating efficient degradation (64 percent) of the MB. Notably, this method offers a novel technique for improving the photocatalytic performance of MOFs, which might be used as a photocatalyst. They found that Zn microcrystals are fantastic support for TiO_2 catalyst loading, resulting in the creation of TiO_2@ZnMOF core-shell exhibiting excellent yields (64%) and selectivity in the photocatalytic destruction of MB. The significant flexibility of this method, as well as the efficient catalytic features of the produced materials, will undoubtedly enhance the field of functional materials research.

Buasakun *et al.* (2021) synthesized the composite of ZnO and MOF-46(Zn) to increase the photocatalytic efficiency of zinc oxide and demonstrate the synergistic theory that exhibited the presence of MOF-46(Zn) and ZnO, offering higher results than pure ZnO. That nanostructures compound had been created by reacting prepared ZnO with 2-aminoterephthalic acid (2-ATP) as a ligand and coating the ZnO surface with MOF-46 (Zn). Pyrolysis of different shapes of IRMOF-3(Zn-MOF) produced using CTAB as a morphological inhibitor was used to modify the ZnO reactant materials. The photodegradation efficiency of the octahedral ZnO produced at 150 mg of CTAB is superior, with 85.79 percent degradation in 180 minutes and bandgap energy of 3.11 eV. In the manufacturing of ZnO@MOF-46, it is utilized as a precursor material (Zn). In the MB degradation reaction, the performance of the ZnO/MOF-46(Zn) hybrid as a photocatalyst compound was compared to that of pure manufactured ZnO. Heterostructure with 61.20 percent in the MB degradation is greater than pure zinc oxide within 1 hour (90.09 percent within 180 min). These findings might be explained by the presence of ZnO and MOF-46(Zn), which allow them to absorb a broader spectrum of energy and reduce the possibility of electron-hole recombination.

5.2. Methyl orange

Azo dyes, a broad category of colorants, account for over half of all dyes used in the textile dyes used. Because azo linkage reduction produces potentially carcinogenic aromatic compounds, the release of industrial effluents from textile factories has produced major environmental pollution concerns. Textile wastewaters containing azo dyes are resistant to standard treating wastewater due to the toxicity of azo dyes, stability, and the existence of persistent surfactants and some other harmful additives (Chen *et al.* 2008). MO is among the most common azo dyes. In conclusion, total methyl orange decomposition from water seems very important and necessary (Yadav *et al.* 2022).

Herrera *et al.* created a novel semicrystalline MOF from zinc nitrate and terephthalic acid reported a complete analysis of its chemical and physical features. Zn-BDC was studied in 3 application fields: adsorption/photocatalytic degradation of MO and MB, as well as the evolution of H_2. MO has the greatest adsorption performance, with an increase in the adsorbent dose of 2,100 mg/g, which is more than the capacity of any of the MOFs mentioned in the study. For the evolution of H_2, catalytic efficiency using MO adsorption was increased 24 times, while the activity of the photocatalyst with MB adsorbed was increased 27 times (from 47 to 1,148 and 1,259 mol/g, respectively). This is due to improved light adsorption and a reduction in charge recombination. Zn-BDC MOF is an efficient anionic dye adsorbent, with the greatest constant rates and adsorption capacity for a MOF reported to date: 2.34×10^{-2} g/min and 2,100 mg/g. The high electrostatic interaction, indicated in a negative Gibbs free energy of 20.115 kJ/mol, is due to Zn-BDC MOF's extraordinary affinity for MO degradation. Because of its simple synthesis technique, inexpensive cost, and outstanding photocatalytic hydrogen development and adsorption performance, BDC-Zn MOF is a suitable choice for use in an industrial process. The mechanism of MO photocatalytic degradation was investigated. As previously mentioned, MO adsorption is mediated by electrostatic repulsion, that encourages connection among BDC-Zn and the color and could lead to increased decomposition. BDC-Zn-MO is adsorbed under solar intensity in the first step as a result of MO's presence. When charged particles move from the conduction band (HOMO orbital analog) to the valence band (LUMO orbital analog), electrons and holes are created. These particles interact with solution to form the oxidizing species •OH, which attacks MO and produces a number of precursors. Eventually, MO is reduced to its simplest constituents, such as CO_2 and water. Contrarily, the band gap value was added to the conduction band to calculate the valence band potential, which resulted in 3.4 eV, which is sufficient for water oxidation (1.23 eV) and the manufacturing of OH (2.4 eV), the 2nd kinds involved in organic chemical breakdown (Herrera *et al.* 2020).

Ghourchian *et al.* developed an innovative and simple method for manufacturing a magnetic $Zn_2(BDC)_2(DABCO)$ MOF as a Fenton-like heterogeneous nano-catalyst for azo dyes degradation in aqueous systems. The MOF-chitosan-Fe_3O_4 nanocomposite (NC) was described in this study for MO degradation. In this study, Draper Lin tiny composite structure and RSM strategies were used to explore and improve the effects of four variables, including the amount of MOF-chitosan-Fe_3O_4 nano-catalyst, preparation time, reaction temperature, and H_2O_2 amount. To determine the ideal conditions for MO reduction by MOF-chitosan-Fe_3O_4 nano-catalyst, statistical analysis and Statgraphics software were used to conduct the SCD on seventeen randomly selected studies. The results of a few initial and prior experimental studies were used to determine the parameters' medium and big values. By using and fitting a second-order polynomial design, the SCD enabled the procured reaction to be styled. The determination coefficient (R^2) was used to evaluate the polynomial model's fitness. The R^2 (99.95%) and adjusted R^2 (99.75%) values demonstrate that the proposed model is suitable for forecasting MO color removal effectiveness in an aqueous environment. An acceptable illustration of the scientific results was provided by the residuals histogram and normally distributed graph, which both showed that the residuals seemed to have a normally distributed. Under optimal conditions, the removal efficiencies of MO using MOF chitosan-Fe_3O_4 nano-catalyst seems to have been >99 percent. The findings indicated that the magnetic MOF might be a suitable recyclable magnetic nano-catalyst for the colored treatment of wastewater. Furthermore, as is well known, kinetics analysis provides important information about the mechanism of removal, so three kinetics models were investigated in this study to better understand the path of MO decolorization. The pseudo-first-order, pseudo-second-order, and Bangham methods were used to analyze the observational evidence. The correlation coefficient (R^2) for pseudo-first order, pseudo second order, and Bangham models was 0.971, 0.995, and 0.898, respectively, according to the outcomes of kinetic data analysis utilizing three 3 different models. According to these findings, the decolorization of MO follows the pseudo-second-order (PSO) model, as evidenced by the kinetics modeling data. This theory is supported by the strong correlation coefficient ($R2 = 0.995$) (Ghourchian *et al.* 2021).

5.3. Crystal violet (methyl violet)

One of the most often used organic dyes is crystal violet (CV), a common organic dye with a triphenylmethane chemical structure observed in so many sewage effluents discharges (Aggarwal *et al.* 2020). CV, a cationic dye, may also be used in industrial diagnostics and medical because of its ability to interact with several other compounds. On the other hand, excessive inhalation of CV dye may cause vomiting, mucous membrane damage, respiratory tract irritation, genetic mutation, dizziness, and diarrhea (Drumm *et al.* 2021). As a result, sophisticated treatment strategies for removing these dangerous compounds from the environment are critical (Soni *et al.* 2020b).

Wang *et al.* synthesized two innovative Zn(II) MOFs with supramolecular isomerism by mixing 1,3-bis(2-methylimidazolyl) propane (bmp) and 1,3,5-benzenetricarboxylic acid (H_3BTC). $[NH_2(CH_3)_2][Zn_2O(bmp)(BTC)]$ is one of the isomers (1) Use a

two-fold interlayer framework structure described by the bey-type of interdependence, whereas one of the other isomer $[NH_2(CH_3)_2][Zn_2O(bmp\ (BTC)]$. 1.5DMF (2) employs a two-fold interlayer framework structure described by CdSO4-type interdependence. That flexibility of the ligand 1,3 bis(2-methylimidazolyl)propane, which causes 2 lies to be on a crystallographic mirror plane, might explain the variation in structures of both MOFs. The two MOFs exhibit significant photocatalytic capabilities for the photodegradation of MV, a typical aromatic dye. In addition, the band gap energies (Eg) of both isomeric MOFs were estimated using DRS at room temperature conditions to make a preliminary assessment of their suitability as photocatalysts. Both MOFs have semiconducting behavior, according to DRS results, with Eg values of 3.63 eV for 1 and 3.96 eV for 2. Both MOFs could be used as photocatalysts based on their band gap parameters. Kinetic analysis was also done on the photocatalysis response of the MV pigment in the existence of the these isomeric Zn(II)-MOFs. According to the kinetic measurements, both photodegradation phenomena follow a pseudo-first-order kinetic model, as evidenced by a linear plot of lnC vs. reaction time t. For 1, k and its square of correlation coefficient parameter R^2 are 0.01176 min1 and 0.9757, respectively, whereas, for 2, k and R^2 are 0.02003 min1 and 0.98853 (Wang *et al.* 2021c).

Jin *et al.* (2017) used asymmetrical rigid carboxylate ligand, terphenyl-3,3′′,5,5′′ tetracarboxylic acid (H_4L), to create a novel MOF, formulated as $([Zn_2IJL)IJDMF)_3]\cdot 2DMF\cdot 2H_2O)$ (1). A 3D uninodal 4-c lonsdaleite (lon) structure based on binuclear Zn clusters is revealed by a single-crystal XRD investigation. The photocatalytic activities of 1 have been investigated for the degradation of MV and RhB. The formation of holes on the Zn(II) cores corresponds to its redox, allowing them to oxidation the color and reduction back to Zn(II), finally decomposing the organic dye.

[Zn (bpe)(fdc)] is a novel MOF reported by Alamgir *et al.* using solvothermal circumstances, 2DMF (BUT-206, bpe = 1,2-bis(4-pyridyl) ethylene, H_2fdc = 2,5-furan dicarboxylic acid, DMF = N,N-dimethylformamide) was synthesized and used for photocatalytic dye degradation such as RhB and CV. Under UV irradiation, BUT-206 demonstrated strong photocatalytic potential in the decomposition of CV without the use of any cocatalysts or photosensitizers. The photodegradation of CV by BUT-206 took just 120 minutes and had a 92.5 percent removal efficiency. The impacts of important factors such as initial dye concentration, photocatalyst quantity, and pH on CV degradation procedures were investigated. The pseudo-first-order kinetic equation was then used to predict the dye degradation kinetics. BUT-206 also showed high photocatalytic activity reusability for up to 5 cycles, indicating that it could be used as a green photocatalists for decolorization. Recyclability of the BUT-206 photocatalyst is a critical factor in cost- and environmentally-conscious sewage purification. The recyclability of BUT-206 was investigated over five periods to see if it was feasible. The suspension was centrifuged after that period and then cleaned multiple times with distilled water, acetone, and ethanol in that order. The procedure was as follows: the revived specimen was sonicated for a brief period of time in a vial containing 5 mL of solvent before being filtered. The repaired product was dried at a vacuum condition before being used in the next cycle. The photocatalytic performance of the MOF sample was investigated over five cycles. After five consecutive cycles, the degradation efficiency decreased slightly, might be the result of contaminants' molecules adhering permanently to the catalyst's catalytic activity. The findings confirmed that while the reactions altered the structure of the MOF, the photocatalytic performance was virtually unchanged (Talha *et al.* 2021).

5.4. Rhodamine B

RhB, one of the most hazardous dyes in textile effluent, has a high value in the textile industry as a textile dye due to its non-biodegradability and great stability. dye lasers, paints, ball pens, carbon stamp pad inks, leather, and crackers explosions are all made with RhB (Al-Gheethi *et al.* 2022). In addition, RhB dye is recognized as a neurotoxic and carcinogenic dye that causes gastrointestinal tract irritation, skin irritation, respiratory tract infection, and toxicity in animals and humans throughout development and simulation. Inhalation and ingestion of RhB are hazardous, causing liver and thyroid damage, as well as eye and skin irritation (Bhat *et al.* 2020).

Polyoxometalate-based metal-organic framework (POMOF) is a challenge as photocatalytic degraders of organic contaminants. To that aim, Wang *et al.* created a new structure of silver borotungstate and zinc homobenzotrizoate ($[Zn_4(BTC)_2(4\text{-}OH_2O)_2]@Ag_5[BW_{12}O_{40}]$ core-shell, shortened as Zn-BTC@$Ag_5[BW_{12}O_{40}]$, BTC1,3,benzylcarboxylic acid) by enveloping polyoxometalate (POM) over MOF using an easy milling approach. For MB, MO, and RhB dyes, the photodegradation performance of Zn-BTC@$Ag_5[BW_{12}O_{40}]$ is higher than 90% in 140 minutes. After 5,000 cycles, the capacitance retention rate was higher than 91 percent. Furthermore, on RhB, MO, and MB dyes, the efficiency of photocatalytic degradation of ZnBTC@$Ag_5[BW_{12}O_{40}]$ core-shell is 91.1 percent, 95.2 percent, and 96.1 percent, respectively. On the other hand, Its

photocatalytic cycle experiments were repeated five times, and the observation revealed negligible variation, suggesting that it may be employed as a suitable photocatalytic compound (Wang *et al.* 2022e).

Zhang *et al.* used a one-step solvothermal technique and calcination of MOFs as supporting material in air to generate hierarchical double-shelled NiO/ZnO hollow spheres heterojunctions. The photocatalytic efficiency of the created compounds for the photodegradation of rhodamine B was also examined using UV–vis light irradiation. The NiO/ZnO microsphere has a remarkable hierarchically porous structure with a core and a shell. The photocatalytic findings revealed that NiO/ZnO hollow spheres had significant catalytic activity for RhB degradation, producing full disintegration of RhB (200 mL of 10 g/L) after 3 hours when exposed to UV–vis light. Additionally, using mass spectroscopy (LC-MS) and liquid chromatography, the degradation mechanism was suggested based on the intermediates produced during the degradation reaction. Hydroxide ions (•OH), the major metabolism component in RhB photodegradation, are responsible for the pollutant's destruction. This study presents an effective and simple method for fabricating porous metal oxide heterojunctions with excellent photocatalytic activity, which could also be applied in pollutants removal.

The two main pathways for its degradation in theory are the direct oxidation of RhB by photogenerated holes and the response with superoxide or hydroxyl radical from photodegradation. The identification of the active material in photocatalytic process is crucial for determining the reaction mechanism. Isopropanol was being used as the greatest hydroxyl radical scrounger because of its significant rate fixed value for reacting with OH^- ions. This allows everyone to evaluate whether superoxide radicals, holes or radical dot OH radicals are responsible for the target's deterioration. RhB degradation was significantly inhibited when 100 mM isopropanol had been introduced to the RhB suspension. The finding demonstrated that the OH^- ions was critical in the RhB oxidation reaction mechanism.

In the photocatalytic process, electron transfer (Tan *et al.* 2022b, 2022c) or photogenerated holes may produce hydroxyl radicals (radical dot OH). In order to determine the generation path of radical dot OH radicals, methanol, an impactful hole scrapper, was provided to the strategies to quench the photogenerated holes in the uv irradiation NiO/ZnO spherical particles. The addition of 100 mM methanol stopped RhB from degrading. It means that the photogenerated hole reaction produced the majority of the radical dot OH radicals (Zhang *et al.* 2018c).

By heating $ZnCl_2$ and H_3BTC in dimethylformamide at pH 8.2, Sarkar *et al.* created a porosity MOF, $[(Zn_3(BTC)_2(H_2O)_3)_2.5H_2O]_n$($H_3BTC = 1,3,5$-benzenetricarboxylic acid). The 3D polymeric unit built by paddlewheel SBUs is shown by a single-crystal XRD investigation. In both water and hexane medium, the prepared MOF exhibits significant iodine absorption (84 percent and 74 percent, respectively). Under visible light and in the presence of H_2O_2, the synthesized MOF shows heterogeneous photocatalytic efficiency for MB (degradation efficiency 79%) and RhB (degradation efficiency 85%) (Sarkar *et al.* 2020).

5.5. Other pollutants

The anionic bi-functional hetero color containing an azo chromophore, Reactive Yellow 145 (RY 145), is commonly used in the dyeing of polyester blended fabrics, polyester, and cotton, as well as in tannery and printing facilities. RY 145 with the cellulose hydroxyl group interacts in two ways: through nucleophilic replacement of reactive chlorine atoms (monochlorotriazine group) or nucleophilic attachment to the active double bond (sulphatoethylsulphone group) (Franck *et al.* 2014). The existence of these two reactive intermediates improves the light fastness properties. Nevertheless, their mutagenic and carcinogenic impacts on humans and aquatic life should not be overlooked. As a result, developing techniques to remove it from water, such as photocatalytic degradation, is necessary (Patil & Shukla 2015).

Nguyen *et al.* (2021) developed Ag_x-Zn_{100-x}-BTC/GO nanostructures (BTC: benzene-1,3,5 tricarboxylic, GO: graphene oxide) with varied Ag/Zn molar concentration ratios using hydrothermal-assisted microwave processing. When compared to Zn-BTC/GO and AgBTC/GO, the Ag_x-Zn_{100-x}-BTC/GO showed exceptional photocatalytic properties in the destruction of RY 145 dye under visible light illumination, with about 100% RY-145 degradation during 0.5 hours. The h^+ and $O_2^{-\bullet}$ are important factors in the RY-145 decomposition in experiments for scavenging reactive oxygen species. The influence of dye concentration, pH, and catalyst dose on the effectiveness of bimetallic Ag_{50}-Zn_{50}-BTC/GO photocatalytic activity was also studied. The photocatalytic reaction was also repeated four times to confirm the stability of Ag50-Zn50-BTC/GO. The performance of eliminating RY-145 stayed constant after four reaction cycles, demonstrating the excellent stability and reusability of the Ag50-Zn50-BTC/GO components' photocatalytic performance. Furthermore, morphology and phase structure is not changed in XRD patterns or SEM images. As a result, the photocatalytic performance of the Ag50-Zn50-BTC/GO photocatalyst is extremely stable.

The existence of chlorinated chemicals in aquatic environments has resulted in several pollution issues. 2-chlorophenol (2-CP) is an example of a chemical in this category (Barakat *et al.* 2005). 2-CP is one of 129 water-related major environmental pollutants that are generated as a result of chemical degradation of pesticides and chlorinated aromatic. It is very hazardous and persistent, causing skin irritation, carcinogenicity, and gastrointestinal difficulties, and poses a severe ecological concern in some circumstances as an environmental contaminant (Mondal & Sabir 2011).

Surib *et al.* (2017) attempted to prepare a novel Cd-linked MOF by an ecofriendly hydrothermal approach. The Cd-daylight-utilizing MOF's properties were improved by using an ion-exchange method to intercalate Ag^{+}, Fe^{3+}, and Zn^{2+} into the structure. Fe^{3+} stimulates the photoreaction in the visible range, whereas Ag^{+} and Zn^{2+} stimulate the photoreaction in the ultraviolet light area, according to the optical properties. Degradation of 2-CP under sunlight illumination was used to examine the photocatalytic effectiveness of the produced MOFs. In comparison to the other prepared compounds, the Cd-MOFs intercalated with Fe^{3+} had remarkable photocatalysis, degrading 93 percent of 2-CP in 5 hours of irradiation. Consequently, when compared to current conventional photocatalysts, the produced modified MOF significantly showed its potential as a sunlight photocatalyst. Cd–, Fe–, Ag–, and Zn–Cd–MOF reusability was investigated. The photocatalysts were reused three times and the efficiency did not change when compared to the virgin cycle. Cryptographic analysis was performed on the recovered MOF to determine its structural stability. The spectra obtained before and after photocatalysis experiments are similar, and the MOFs are the same, indicating that their structures are not distorted during photocatalysis experiments conducted under daylight illumination. The study established the studied MOF's robust stability.

6. CONCLUSION

MOFs are being investigated at a quick rate due to their structural features, which are leading to the development of novel frameworks, and their usage in photocatalysis degradation has increased over the last decade. In many ways, Zn-MOFs perform like a microporous semiconductor that is stable to illumination, and it can develop charge-separated and create a large number of electron-hole pairs. Charge separation happens as a result of light absorption on the ligand-to-metal charge transfer band. The obvious increasing trend in the number of articles published on this topic reflects the scholarly community's interest in this area. In this review, the general structure, synthesis methods, and photocatalytic activity of Zn-MOFs and their composite have been discussed. The reviews show that MOFs have been successfully applied for photocatalytic degradation of a several of organic contaminants in water such as MB, MO, CV, and RhB. Therefore, Zn-MOFs nanocomposites are suitable photocatalytic materials for wastewater purification soon. The improvement in efficiency and stability should be attributed to the efficient removal and transition of photogenerated charges coming from carefully contacted connections with well-matched interleaved band structures. A flexible method for enhancing the production and stability of catalysts is to couple semiconductor material with well-matched band energy sources. This method also offers ideas for the design and fabrication of other extremely chemically stable components. This paper discussed the stability of photocatalysts used to degrade the mentioned pollutants. The results showed excellent and impressive stability of metal-organic frameworks based on Zn.

ETHICS APPROVAL

Not applicable.

CONSENT TO PARTICIPATE AND CONSENT TO PUBLISH

Not applicable.

AUTHOR CONTRIBUTION

All authors conceived of the study, performed the research, helped analyze data, and drafted the manuscript and helped perform the research, analyze data, and reviewed the chart. All authors read and approved the manuscript. The authors declare that all data were generated in-house and that no paper mill was used.

FUNDING

The authors declare that no funds, grants, or other support were received during the preparation of this manuscript.

DATA AVAILABILITY STATEMENT

All relevant data are included in the paper or its Supplementary Information.

CONFLICT OF INTEREST

The authors declare there is no conflict.

REFERENCES

Abdelhameed, R. M. & Emam, H. E. 2022 Modulation of metal organic framework hybrid cotton for efficient sweeping of dyes and pesticides from wastewater. *Sustainable Materials and Technologies* **31**, e00366.

Abdelhameed, R. M. *et al.* 2021a Efficient elimination of chlorpyrifos via tailored macroporous membrane based on Al-MOF. *Sustainable Materials and Technologies* **29**, e00326.

Abdelhameed, R. M. *et al.* 2021b Temperature-controlled-release of essential oil via reusable mesoporous composite of microcrystalline cellulose and zeolitic imidazole frameworks. *Journal of Industrial and Engineering Chemistry* **94**, 134–144.

Abdelhameed, R. M., Abdel-Gawad, H. & Emam, H. E. 2021c Macroporous Cu-MOF@ cellulose acetate membrane serviceable in selective removal of dimethoate pesticide from wastewater. *Journal of Environmental Chemical Engineering* **9** (2), 105121.

Abdelhameed, R. M. *et al.* 2022 Purification of soybean oil from diazinon insecticide by iron-based metal organic framework: effect of geometrical shape and simulation study. *Journal of Molecular Structure* **1250**, 131914.

Abdollahi, N. *et al.* 2018 Sonochemical synthesis and structural characterization of a new Zn (II) nanoplate metal–organic framework with removal efficiency of Sudan red and Congo red. *Ultrasonics Sonochemistry* **45**, 50–56.

Abuzalat, O. *et al.* 2018 Sonochemical fabrication of Cu (II) and Zn (II) metal-organic framework films on metal substrates. *Ultrasonics Sonochemistry* **45**, 180–188.

Aggarwal, R. *et al.* 2020 Bitter apple peel derived photoactive carbon dots for the sunlight induced photocatalytic degradation of crystal violet dye. *Solar Energy* **197**, 326–331.

Ahmed, B. *et al.* 2020 Destruction of cell topography, morphology, membrane, inhibition of respiration, biofilm formation, and bioactive molecule production by nanoparticles of Ag, ZnO, CuO, TiO_2, and Al_2O_3 toward beneficial soil bacteria. *ACS Omega* **5** (14), 7861–7876.

Akbarizadeh, M. R. *et al.* 2022a Cytotoxic activity and magnetic behavior of green synthesized iron oxide nanoparticles on brain glioblastoma cells. *Nanomedicine Research Journal* **7** (1), 99–106.

Akbarizadeh, M. R., Sarani, M. & Darijani, S. 2022b Study of antibacterial performance of biosynthesized pure and Ag-doped ZnO nanoparticles. *Rendiconti Lincei. Scienze Fisiche e Naturali*, 1–9.

Akter, F. *et al.* 2022 Cocos nucifera endocarp extract exhibits anti-diabetic and antilipidemic activities in diabetic rat model. *International Journal of Scientific Research in Dental and Medical Sciences* **4** (1), 8–15.

Alahri, M. B. *et al.* 2021 Theranostic applications of metal–organic frameworks (MOFs)-based materials in brain disorders: recent advances and challenges. *Inorganic Chemistry Communications* **134**, 108997.

Al-Enazi, N. M. *et al.* 2021 Tin oxide nanoparticles (sno2-NPs) synthesis using Galaxaura elongata and its anti-microbial and cytotoxicity study: a greenery approach. *Applied Nanoscience*, 1–9.

Al-Gheethi, A. A. *et al.* 2022 Sustainable approaches for removing Rhodamine B dye using agricultural waste adsorbents: a review. *Chemosphere* **287**, 132080.

Alhomaidi, E. *et al.* 2022 Biosynthesis of silver nanoparticles using Lawsonia inermis and their biomedical application. *IET Nanobiotechnology*.

Alijani, H. Q. *et al.* 2021 Biosynthesis of spinel nickel ferrite nanowhiskers and their biomedical applications. *Scientific Reports* **11** (1), 1–7.

Alimadadi, H., Ashraf, H. & Nasrabadi, N. 2019 Dens Invaginatus with palatal expansion and Buccal Sinus tract: a case report. *International Journal of Scientific Research in Dental and Medical Sciences* **1** (3), 52–56.

Aljumaily, M. M. *et al.* 2022 Modification of poly (vinylidene fluoride-CO-hexafluoropropylene) membranes with DES-functionalized carbon nanospheres for removal of methyl orange by membrane distillation. *Water* **14** (9), 1396.

Almansob, A. *et al.* 2022a Effective treatment of resistant opportunistic fungi associated with immuno-compromised individuals using silver biosynthesized nanoparticles. *Applied Nanoscience*, 1–12.

Almansob, A., Bahkali, A. H. & Ameen, F. 2022b Efficacy of gold nanoparticles against drug-resistant nosocomial fungal pathogens and their extracellular enzymes: resistance profiling towards established antifungal agents. *Nanomaterials* **12** (5), 814.

AlNadhari, S. *et al.* 2021 A review on biogenic synthesis of metal nanoparticles using marine algae and its applications. *Environmental Research* **194**, 110672.

Al-Nayili, A. *et al.* 2022 Formic acid dehydrogenation using noble-metal nanoheterogeneous catalysts: towards sustainable hydrogen-based energy. *Catalysts* **12** (3), 324.

Alsamhary, K. *et al.* 2020 Gold nanoparticles synthesised by flavonoid tricetin as a potential antibacterial nanomedicine to treat respiratory infections causing opportunistic bacterial pathogens. *Microbial Pathogenesis* **139**, 103928.

Alshehrei, F., Al-Enazi, N. M. & Ameen, F. 2021 Vermicomposting amended with microalgal biomass and biochar produce phytopathogen-resistant seedbeds for vegetables. *Biomass Conversion and Biorefinery*, 1–8.

Alwin, S., Ramasubbu, V. & Shajan, X. S. 2018 $$\hbox {TiO} _ {2} $$ TiO_2 aerogel–metal organic framework nanocomposite: a new class of photoanode material for dye-sensitized solar cell applications. *Bulletin of Materials Science* **41** (1), 1–8.

AlYahya, S. *et al.* 2018 Size dependent magnetic and antibacterial properties of solvothermally synthesized cuprous oxide (cu2o) nanocubes. *Journal of Materials Science: Materials in Electronics* **29** (20), 17622–17629.

Ameen, F. 2022 Optimization of the synthesis of fungus-mediated bi-metallic Ag-Cu nanoparticles. *Applied Sciences* **12** (3), 1384.

Ameen, F. *et al.* 2018 Flavonoid dihydromyricetin-mediated silver nanoparticles as potential nanomedicine for biomedical treatment of infections caused by opportunistic fungal pathogens. *Research on Chemical Intermediates* **44** (9), 5063–5073.

Ameen, F. *et al.* 2019 Phytosynthesis of silver nanoparticles using Mangifera indica flower extract as bioreductant and their broad-spectrum antibacterial activity. *Bioorganic Chemistry* **88**, 102970.

Ameen, F. *et al.* 2020a Fabrication of silver nanoparticles employing the cyanobacterium Spirulina platensis and its bactericidal effect against opportunistic nosocomial pathogens of the respiratory tract. *Journal of Molecular Structure* **1217**, 128392.

Ameen, F. *et al.* 2020b Soil bacteria Cupriavidus sp. mediates the extracellular synthesis of antibacterial silver nanoparticles. *Journal of Molecular Structure* **1202**, 127233.

Ameen, F. *et al.* 2021a Anti-oxidant, anti-fungal and cytotoxic effects of silver nanoparticles synthesized using marine fungus Cladosporium halotolerans. *Applied Nanoscience*, 1–9.

Ameen, F., Dawoud, T. & AlNadhari, S. 2021b Ecofriendly and low-cost synthesis of ZnO nanoparticles from Acremonium potronii for the photocatalytic degradation of azo dyes. *Environmental Research* **202**, 111700.

Ameen, F. *et al.* 2022 Antioxidant, antibacterial and anticancer efficacy of Alternaria chlamydospora-mediated gold nanoparticles. *Applied Nanoscience*, 1–8.

Amiri, H. *et al.* 2020 Translation and adaptation of the posttraumatic growth inventory-short form into Persian. *The Open Psychology Journal* **13** (1).

Amiri, H. *et al.* 2021a Patterns of traumatic events and its relations with posttraumatic growth and religiosity in Iranian college students. *Journal of Education and Health Promotion* **10**.

Amiri, H. *et al.* 2021b Posttraumatic growth after earthquake: a systematic review and meta-analysis. *International Journal of Social Psychiatry* **67** (7), 867–877.

Amiri, H. *et al.* 2022 Latent profiles of posttraumatic growth: 17 years after the Bam earthquake in Iran. *Disaster Medicine and Public Health Preparedness*, 1–6.

Arkaban, H. *et al.* 2022 Polyacrylic acid nanoplatforms: antimicrobial, tissue engineering, and cancer theranostic applications. *Polymers* **14** (6), 1259.

Arora, C. *et al.* 2019 Iron based metal organic framework for efficient removal of methylene blue dye from industrial waste. *Journal of Molecular Liquids* **284**, 343–352.

Arora, C. *et al.* 2021 Chapter 14 - dye removal from waste water using metal organic frameworks. In: *Management of Contaminants of Emerging Concern (CEC) in Environment* (Singh, P., Hussain, C. M. & Rajkhowa, S., eds). Elsevier, pp. 375–394.

Ashpazzadeh, E. *et al.* 2022 Hermite multiwavelets representation for the sparse solution of nonlinear Abel's integral equation. *Applied Mathematics and Computation* **427**, 127171.

Assi, L. N. *et al.* 2021 Early properties of concrete with alkali-activated fly ash as partial cement replacement. *Proceedings of the Institution of Civil Engineers – Construction Materials* **174** (1), 13–20.

Au, K. M. *et al.* 2016 Folate-targeted pH-responsive calcium zoledronate nanoscale metal-organic frameworks: turning a bone antiresorptive agent into an anticancer therapeutic. *Biomaterials* **82**, 178–193.

Awad, E. S. *et al.* 2022 Groundwater hydrogeochemical and quality appraisal for agriculture irrigation in Greenbelt area, Iraq. *Environments* **9** (4), 43.

Bagheri, N. *et al.* 2018 Mimetic Ag nanoparticle/Zn-based MOF nanocomposite (AgNPs@ ZnMOF) capped with molecularly imprinted polymer for the selective detection of patulin. *Talanta* **179**, 710–718.

Bai, B. *et al.* 2021 Cotransport of heavy metals and SiO2 particles at different temperatures by seepage. *Journal of Hydrology* **597**, 125771.

Barakat, M. *et al.* 2005 Photocatalytic degradation of 2-chlorophenol by Co-doped TiO_2 nanoparticles. *Applied Catalysis B: Environmental* **57** (1), 23–30.

Barani, M. *et al.* 2020 Nanotreatment and nanodiagnosis of prostate cancer: recent updates. *Nanomaterials* **10** (9), 1696.

Barani, M. *et al.* 2021a Nanotechnology in ovarian cancer: diagnosis and treatment. *Life Sciences* **266**, 118914.

Barani, M. *et al.* 2021b Recent advances in nanotechnology-based diagnosis and treatments of human osteosarcoma. *Biosensors* **11** (2), 55.

Bazi Alahri, M. *et al.* 2021 Theranostic applications of metal–organic frameworks (MOFs)-based materials in brain disorders: recent advances and challenges. *Inorganic Chemistry Communications* **134**, 108997.

Begum, I. *et al.* 2021 Facile fabrication of malonic acid capped silver nanoparticles and their antibacterial activity. *Journal of King Saud University-Science* **33** (1), 101231.

Begum, I. *et al.* 2022 A combinatorial approach towards antibacterial and antioxidant activity using tartaric acid capped silver nanoparticles. *Processes* **10** (4), 716.

Bhat, S. A. *et al.* 2020 Highly efficient catalytic reductive degradation of Rhodamine-B over Palladium-reduced graphene oxide nanocomposite. *Chemical Physics Letters* **754**, 137724.

Bilal, M. *et al.* 2020 Nanomaterials for the treatment and diagnosis of Alzheimer's disease: an overview. *NanoImpact* **20**, 100251.

Buasakun, J. *et al.* 2021 Synthesis of heterostructure of ZnO@ MOF-46 (Zn) to improve the photocatalytic performance in methylene blue degradation. *Crystals* **11** (11), 1379.
Byrappa, K. & Yoshimura, M. 2012 *Handbook of Hydrothermal Technology*. William Andrew.
Cao, Y. *et al.* 2021a Green synthesis of bimetallic ZnO–CuO nanoparticles and their cytotoxicity properties. *Scientific Reports* **11** (1), 23479.
Cao, Y. *et al.* 2021b K-doped ZnO nanostructures: biosynthesis and parasiticidal application. *Journal of Materials Research and Technology* **15**, 5445–5451.
Cao, Y. *et al.* 2022 Ceramic magnetic ferrite nanoribbons: eco-friendly synthesis and their antifungal and parasiticidal activity. *Ceramics International* **48** (3), 3448–3454.
Chen, H. & Wang, Q. 2021 Regulatory mechanisms of lipid biosynthesis in microalgae. *Biological Reviews* **96** (5), 2373–2391.
Chen, W. & Wu, C. 2018 Synthesis, functionalization, and applications of metal–organic frameworks in biomedicine. *Dalton Transactions* **47** (7), 2114–2133.
Chen, Y.-P. *et al.* 2008 Radiation-induced degradation of methyl orange in aqueous solutions. *Chemosphere* **72** (4), 532–536.
Chen, C.-X. *et al.* 2021a Non-covalent self-assembly synthesis of AQ2S@ rGO nanocomposite for the degradation of sulfadiazine under solar irradiation: the indispensable effect of chloride. *Applied Catalysis B: Environmental* **298**, 120495.
Chen, L. *et al.* 2021b Corynoxine protects dopaminergic neurons through inducing autophagy and diminishing neuroinflammation in rotenone-induced animal models of Parkinson's disease. *Frontiers in Pharmacology* **12**, 363.
Chen, F. *et al.* 2022 Biodegradation performance and anti-fouling mechanism of an ICME/electro-biocarriers-MBR system in livestock wastewater (antibiotic-containing) treatment. *Journal of Hazardous Materials* **426**, 128064.
Chu, Y. & Zhao, T. 2016 Concavity of the error function with respect to Hölder means. *Mathematical Inequalities & Applications* **19** (2), 589–595.
Chu, H.-H., Zhao, T.-H. & Chu, Y.-M. 2020 Sharp bounds for the Toader mean of order 3 in terms of arithmetic, quadratic and contraharmonic means. *Mathematica Slovaca* **70** (5), 1097–1112.
Chu, Y.-M. *et al.* 2021 Enhancement in thermal energy and solute particles using hybrid nanoparticles by engaging activation energy and chemical reaction over a parabolic surface via finite element approach. *Fractal and Fractional* **5** (3), 119.
Chu, Y.-M. *et al.* 2022a Combined impact of Cattaneo-Christov double diffusion and radiative heat flux on bio-convective flow of Maxwell liquid configured by a stretched nano-material surface. *Applied Mathematics and Computation* **419**, 126883.
Chu, Y. M. *et al.* 2022b Model-based comparative study of magnetohydrodynamics unsteady hybrid nanofluid flow between two infinite parallel plates with particle shape effects. *Mathematical Methods in the Applied Sciences*.
Dai, L. *et al.* 2022a Pollution characteristics and source analysis of microplastics in the Qiantang River in southeastern China. *Chemosphere* **293**, 133576.
Dai, J. *et al.* 2022b Electrochemical degradation of antibiotic enoxacin using a novel PbO_2 electrode with a graphene nanoplatelets interlayer: characteristics, efficiency and mechanism. *Chemosphere* **307**, 135833.
Dang, L.-L. *et al.* 2014 A new acylamide MOF showing uncommon ten-fold interpenetration. *Inorganic Chemistry Communications* **45**, 30–32.
Dang, Y. T. *et al.* 2020 Room temperature synthesis of biocompatible nano Zn-MOF for the rapid and selective adsorption of curcumin. *Journal of Science: Advanced Materials and Devices* **5** (4), 560–565.
Dang, L.-L. *et al.* 2022 Stable zinc-based metal-organic framework photocatalyst for effective visible-light-driven hydrogen production. *Molecules* **27** (6), 1917.
de Lima Neto, O. J. *et al.* 2019 Rapid and efficient electrochemical synthesis of a zinc-based nano-MOF for Ibuprofen adsorption. *New Journal of Chemistry* **43** (14), 5518–5524.
Dong, H. & Koenig, G. M. 2020 A review on synthesis and engineering of crystal precursors produced via coprecipitation for multicomponent lithium-ion battery cathode materials. *CrystEngComm* **22** (9), 1514–1530.
Drumm, F. C. *et al.* 2021 Macro-fungal (Agaricus bisporus) wastes as an adsorbent in the removal of the acid red 97 and crystal violet dyes from ideal colored effluents. *Environmental Science and Pollution Research* **28** (1), 405–415.
Ebrahimi, A. K., Barani, M. & Sheikhshoaie, I. 2018 Fabrication of a new superparamagnetic metal-organic framework with core-shell nanocomposite structures: characterization, biocompatibility, and drug release study. *Materials Science and Engineering: C* **92**, 349–355.
Emam, H. E., Abdelhameed, R. M. & Ahmed, H. B. 2020 Adsorptive performance of MOFs and MOF containing composites for clean energy and safe environment. *Journal of Environmental Chemical Engineering* **8** (5), 104386.
Emam, H. E., El-Shahat, M. & Abdelhameed, R. M. 2021 Observable removal of pharmaceutical residues by highly porous photoactive cellulose acetate@ MIL-MOF film. *Journal of Hazardous Materials* **414**, 125509.
Endriani, R. *et al.* 2022 Aerobic bacteria and antibiotic sensitivity on odontectomy wound in RSUD Arifin Achmad Riau. *International Journal of Scientific Research in Dental and Medical Sciences* **4** (1), 26–32.
Erwei, S. *et al.* 1996 Development and application of hydrothermal method. *Journal of Inorganic Materials* **2**.
Fauzi, A. *et al.* 2022 A critical review on relationship of CeO2-based photocatalyst towards mechanistic degradation of organic pollutant. *Chemosphere* **286**, 131651.
Fiévet, F. *et al.* 2018 The polyol process: a unique method for easy access to metal nanoparticles with tailored sizes, shapes and compositions. *Chemical Society Reviews* **47** (14), 5187–5233.
Firouzeh, N. *et al.* 2021 Degradation of ciprofloxacin using ultrasound/ZnO/oxone process from aqueous solution-lab-scale analysis and optimization. *BioNanoScience* **11** (2), 306–313.

Franck, D. *et al.* 2014 In vitro evaluation of bi-layer silk fibroin scaffolds for gastrointestinal tissue engineering. *Journal of Tissue Engineering* **5**, 2041731414556849.

Gangalla, R. *et al.* 2021 Optimization and characterization of exopolysaccharide produced by Bacillus aerophilus rk1 and its in vitro antioxidant activities. *Journal of King Saud University-Science* **33** (5), 101470.

Gao, T. *et al.* 2019 Dispersing mechanism and tribological performance of vegetable oil-based CNT nanofluids with different surfactants. *Tribology International* **131**, 51–63.

Gao, T. *et al.* 2021 Grindability of carbon fiber reinforced polymer using CNT biological lubricant. *Scientific Reports* **11** (1), 1–14.

Gao, T. *et al.* 2022 Fiber-reinforced composites in milling and grinding: machining bottlenecks and advanced strategies. *Frontiers of Mechanical Engineering* **2022**, 1.

Ge, D. *et al.* 2019 Insight into the enhanced sludge dewaterability by tannic acid conditioning and pH regulation. *Science of The Total Environment* **679**, 298–306.

Ghazal, S. *et al.* 2021 Sol-gel synthesis of selenium-doped nickel oxide nanoparticles and evaluation of their cytotoxic and photocatalytic properties. *Inorganic Chemistry Research* **5** (1), 37–49.

Ghodake, G. S. *et al.* 2018 Colorimetric detection of Cu^{2+}based on the formation of peptide–copper complexes on silver nanoparticle surfaces. *Beilstein J Nanotechnol* **9**, 1414–1422.

Ghourchian, F. *et al.* 2021 Zn-based MOF-chitosan-Fe_3O_4 nanocomposite as an effective nano-catalyst for azo dye degradation. *Journal of Environmental Chemical Engineering* **9** (6), 106388.

Guan, Q. *et al.* 2021 Ultrasonic power combined with seed materials for recovery of phosphorus from swine wastewater via struvite crystallization process. *Journal of Environmental Management* **293**, 112961.

Guo, X. & Wang, J. 2019 Sorption of antibiotics onto aged microplastics in freshwater and seawater. *Marine Pollution Bulletin* **149**, 110511.

Guo, S. *et al.* 2017 Experimental evaluation of the lubrication performance of mixtures of castor oil with other vegetable oils in MQL grinding of nickel-based alloy. *Journal of Cleaner Production* **140**, 1060–1076.

Haghighat, M. *et al.* 2022 Cytotoxicity properties of plant-mediated synthesized K-doped ZnO nanostructures. *Bioprocess and Biosystems Engineering* **45** (1), 97–105.

Hajiashrafi, S. & Kazemi, N. M. 2019 Preparation and evaluation of ZnO nanoparticles by thermal decomposition of MOF-5. *Heliyon* **5** (9), e02152.

Hajiseyedazizi, S. N. *et al.* 2021 On multi-step methods for singular fractional q-integro-differential equations. *Open Mathematics* **19** (1), 1378–1405.

Hashemi, N. *et al.* 2021 Leishmanicidal activities of biosynthesized BaCO3 (witherite) nanoparticles and their biocompatibility with macrophages. *Bioprocess and Biosystems Engineering* **44** (9), 1957–1964.

He, H. *et al.* 2022 Metal–organic framework supported Au nanoparticles with organosilicone coating for high-efficiency electrocatalytic N2 reduction to NH3. *Applied Catalysis B: Environmental* **302**, 120840.

Herrera, L. Á. A. *et al.* 2020 BDC-Zn MOF sensitization by MO/MB adsorption for photocatalytic hydrogen evolution under solar light. *Materials Science in Semiconductor Processing* **109**, 104950.

Hou, L. *et al.* 2019 ZnMOF-74 responsive fluorescence sensing platform for detection of Fe^{3+}. *Microchemical Journal* **150**, 104154.

Hu, X. *et al.* 2018 A signal-on electrochemiluminescence sensor for clenbuterol detection based on zinc-based metal-organic framework–reduced graphene oxide–CdTe quantum dot hybrids. *Analytical and Bioanalytical Chemistry* **410** (30), 7881–7890.

Huang, Y. *et al.* 2019 Preparation of porous graphene/carbon nanotube composite and adsorption mechanism of methylene blue. *SN Applied Sciences* **1** (1), 1–11.

Hussein, A. A. *et al.* 2021 Analysis of relationship between design and implementation stages within construction projects in Iraq. In *IOP Conference Series: Earth and Environmental Science*. IOP Publishing.

Indhira, D. *et al.* 2022 Biomimetic facile synthesis of zinc oxide and copper oxide nanoparticles from Elaeagnus indica for enhanced photocatalytic activity. *Environmental Research* **212**, 113323.

Iqbal, S. A. *et al.* 2022 Dynamical analysis of nonautonomous RLC circuit with the absence and presence of Atangana-Baleanu fractional derivative. *Journal of Applied Analysis & Computation* **12** (2), 770–789.

Iram, S. *et al.* 2017 Gold nanoconjugates reinforce the potency of conjugated cisplatin and doxorubicin. *Colloids and Surfaces B: Biointerfaces* **160**, 254–264.

Isacfranklin, M. *et al.* 2020a Synthesis of highly active biocompatible ZrO2 nanorods using a bioextract. *Ceramics International* **46** (16), 25915–25920.

Isacfranklin, M. *et al.* 2020b Y_2O_3 nanorods for cytotoxicity evaluation. *Ceramics International* **46** (12), 20553–20557.

Isacfranklin, M. *et al.* 2020c Single-phase Cr_2O_3 nanoparticles for biomedical applications. *Ceramics International* **46** (12), 19890–19895.

Jasim, S. A. *et al.* 2022a Investigation of crotonaldehyde adsorption on pure and Pd-decorated GaN nanotubes: a density functional theory study. *Solid State Communications* **348**, 114741.

Jasim, S. A. *et al.* 2022b Nanomagnetic Salamo-based-Pd (0) complex: an efficient heterogeneous catalyst for Suzuki–Miyaura and Heck cross-coupling reactions in aqueous medium. *Journal of Molecular Structure* **1261**, 132930.

Jasim, S. A. *et al.* 2022c Green synthesis of spinel copper ferrite ($CuFe_2O_4$) nanoparticles and their toxicity. *Nanotechnology Reviews* **11** (1), 2483–2492.

Jasni, M. J. F. *et al.* 2017 Fabrication, characterization and application of laccase–nylon 6,6/Fe3 + composite nanofibrous membrane for 3,3′-dimethoxybenzidine detoxification. *Bioprocess and Biosystems Engineering* **40** (2), 191–200.

Jia, D. *et al.* 2014 Experimental verification of nanoparticle jet minimum quantity lubrication effectiveness in grinding. *Journal of Nanoparticle Research* **16** (12), 1–15.

Jia, D. *et al.* 2022 Lubrication-enhanced mechanisms of titanium alloy grinding using lecithin biolubricant. *Tribology International* **169**, 107461.

Jin, J.-C. *et al.* 2017 A 3D luminescent Zn (II) MOF for the detection of high explosives and the degradation of organic dyes: an experimental and computational study. *CrystEngComm* **19** (43), 6464–6472.

Jin, J.-C. *et al.* 2018 A new Zn (ii) metal–organic framework having 3D CdSO4 topology as luminescent sensor and photocatalyst for degradation of organic dyes. *New Journal of Chemistry* **42** (4), 2767–2775.

Jin, F. *et al.* 2022 On nonlinear evolution model for drinking behavior under Caputo-Fabrizio derivative. *Journal of Applied Analysis & Computation* **12** (2), 790–806.

Karthikeyan, K. *et al.* 2021 Almost sectorial operators on Ψ-Hilfer derivative fractional impulsive integro-differential equations. *Mathematical Methods in the Applied Sciences*.

Kausikan, S. P. *et al.* 2022 The impact of COVID-19 on auditory and visual choice reaction time of non-hospitalized patients: an observational study. *International Journal of Scientific Research in Dental and Medical Sciences* **4** (1), 21–25.

Khan, I. A. *et al.* 2014 Porous carbon as electrode material in direct ethanol fuel cells (DEFCs) synthesized by the direct carbonization of MOF-5. *Journal of Solid State Electrochemistry* **18** (6), 1545–1555.

Khan, A. *et al.* 2020 Fabrication and antibacterial activity of nanoenhanced conjugate of silver (I) oxide with graphene oxide. *Materials Today Communications* **25**, 101667.

Khatami, M. & Iravani, S. 2021 Green and eco-friendly synthesis of nanophotocatalysts: an overview. *Comments on Inorganic Chemistry*, 1–55.

Khatami, M. *et al.* 2018 Core@ shell nanoparticles: greener synthesis using natural plant products. *Applied Sciences* **8** (3), 411.

Kim, J. *et al.* 2011 Control of catenation in CuTATB-n metal–organic frameworks by sonochemical synthesis and its effect on CO_2 adsorption. *Journal of Materials Chemistry* **21** (9), 3070–3076.

Kim, D.-Y. *et al.* 2018 Green synthesis of silver nanoparticles using Laminaria japonica extract: characterization and seedling growth assessment. *Journal of Cleaner Production* **172**, 2910–2918.

Kumar, V. *et al.* 2022 Evaluation of cytotoxicity and genotoxicity effects of refractory pollutants of untreated and biomethanated distillery effluent using Allium cepa. *Environmental Pollution* **300**, 118975.

Kurisingal, J. F. *et al.* 2020 Multi-variate metal organic framework as efficient catalyst for the cycloaddition of CO_2 and epoxides in a gas-liquid-solid reactor. *Chemical Engineering Journal* **386**, 121700.

Laurent, S. *et al.* 2008 Magnetic iron oxide nanoparticles: synthesis, stabilization, vectorization, physicochemical characterizations, and biological applications. *Chemical Reviews* **108** (6), 2064–2110.

Li, L. 2021 Synthesis and catalytic properties of metal-organic frameworks mimicking carbonic anhydrase.

Li, B. *et al.* 2016 Grinding temperature and energy ratio coefficient in MQL grinding of high-temperature nickel-base alloy by using different vegetable oils as base oil. *Chinese Journal of Aeronautics* **29** (4), 1084–1095.

Li, N. *et al.* 2019 Simultaneous removal of tetracycline and oxytetracycline antibiotics from wastewater using a ZIF-8 metal organic-framework. *Journal of Hazardous Materials* **366**, 563–572.

Li, K. *et al.* 2020 Removal of tetracycline in sewage and dairy products with high-stable MOF. *Molecules* **25** (6), 1312.

Li, X.-Y. *et al.* 2021a Inverse CO_2/C_2H_2 separation in a pillared-layer framework featuring a chlorine-modified channel by quadrupole-moment sieving. *Separation and Purification Technology* **279**, 119608.

Li, M. *et al.* 2021b MOFs-derived Zn-based catalysts in Acetylene Acetoxylation. *Nanomaterials* **12** (1), 98.

Li, Y. *et al.* 2022a In situ plasma cleaning of large-aperture optical components in ICF. *Nuclear Fusion* **62** (7), 076023.

Li, H. *et al.* 2022b Extreme pressure and antiwear additives for lubricant: academic insights and perspectives. *The International Journal of Advanced Manufacturing Technology*, 1–27.

Li, H. *et al.* 2022c Cutting fluid corrosion inhibitors from inorganic to organic: progress and applications. *Korean Journal of Chemical Engineering*, 1–28.

Liang, H. *et al.* 2020 Pseudocapacitance-dominated high-performance and stable lithium-ion batteries from MOF-derived spinel $ZnCo_2O_4$/ZnO/C heterostructure anode. *Dalton Transactions* **49** (38), 13311–13316.

Ling, P. *et al.* 2019 Metal–organic framework nanosheets with flower-like structure as probes for H 2 S detection and in situ singlet-oxygen production. *Chemical Communications* **55** (45), 6385–6388.

Ling, P. *et al.* 2021 Singlet-oxygen generated by a metal–organic framework for electrochemical biosensing. *Journal of Materials Chemistry B*.

Liu, W. *et al.* 2008 Treatment of CrVI-Containing Mg (OH) 2 nanowaste. *Angewandte Chemie* **120** (30), 5701–5704.

Liu, B. *et al.* 2013 Dynamic Zn-based metal–organic framework: stepwise adsorption, hysteretic desorption and selective carbon dioxide uptake. *Journal of Materials Chemistry A* **1** (22), 6535–6538.

Liu, W. *et al.* 2018 Effective extraction of Cr (VI) from hazardous gypsum sludge via controlling the phase transformation and chromium species. *Environmental Science & Technology* **52** (22), 13336–13342.

Liu, W. *et al.* 2020 Different pathways for Cr (III) oxidation: implications for Cr (VI) reoccurrence in reduced chromite ore processing residue. *Environmental Science & Technology* **54** (19), 11971–11979.

Liu, Y. *et al.* 2021a Comparative study of photocatalysis and gas sensing of ZnO/Ag nanocomposites synthesized by one-and two-step polymer-network gel processes. *Journal of Alloys and Compounds* **868**, 158723.

Liu, K. *et al.* 2021b DeepBAN: a temporal convolution-based communication framework for dynamic WBANs. *IEEE Transactions on Communications* **69** (10), 6675–6690.

Liu, M. *et al.* 2021c Walnut fruit processing equipment: academic insights and perspectives. *Food Engineering Reviews* **13** (4), 822–857.

Liu, M. *et al.* 2021d Cryogenic minimum quantity lubrication machining: from mechanism to application. *Frontiers of Mechanical Engineering* **16** (4), 649–697.

Ma, Z.-P. *et al.* 2022 A dual strategy for synthesizing crystal plane/defect co-modified BiOCl microsphere and photodegradation mechanism insights. *Journal of Colloid and Interface Science* **617**, 73–83.

Mahawar, R. *et al.* 2022 Nasal cavity malignant solitary fibrous tumor: a case report. *International Journal of Scientific Research in Dental and Medical Sciences* **4** (1), 42–44.

Majdi, A. & Vacareanu, R. 2021 Evaluation of seismic damage to Iraqi educational reinforced concrete building using FEMA P-58 methodology. In *IOP Conference Series: Earth and Environmental Science*. IOP Publishing.

Manna, B., Sharma, S. & Ghosh, S. K. 2018 Synthesis and crystal structure of a Zn (II)-based MOF bearing neutral N-donor linker and $SiF6^{2-}$ anion. *Crystals* **8** (1), 37.

Megarajan, S. *et al.* 2022 Synthesis of N-myristoyltaurine stabilized gold and silver nanoparticles: assessment of their catalytic activity, antimicrobial effectiveness and toxicity in zebrafish. *Environmental Research* **212**, 113159.

Mjejri, I. *et al.* 2017 Double-sided electrochromic device based on metal–organic frameworks. *ACS Applied Materials & Interfaces* **9** (46), 39930–39934.

Moghadam, N. C. Z. *et al.* 2022 Nickel oxide nanoparticles synthesis using plant extract and evaluation of their antibacterial effects on Streptococcus mutans. *Bioprocess and Biosystems Engineering* **45** (7), 1201–1210.

Mohammed, A. E. *et al.* 2022 In-silico predicting as a tool to develop plant-based biomedicines and nanoparticles: Lycium shawii metabolites. *Biomedicine & Pharmacotherapy* **150**, 113008.

Mohanta, Y. K. *et al.* 2018 Bio-inspired synthesis of silver nanoparticles from leaf extracts of Cleistanthus collinus (Roxb.): its potential antibacterial and anticancer activities. *IET Nanobiotechnology* **12** (3), 343–348.

Mondal, P. K. & Sabir, S. 2011 Bioremediation of 2-chlorophenol containing wastewater by aerobic granules-kinetics and toxicity. *Journal of Hazardous Materials* **190** (1–3), 222–228.

Moradi, E. *et al.* 2019 A sonochemically-synthesized microporous metal-organic framework for the rapid and efficient ultrasonic-assisted removal of mercury (II) ions in a water solution and a study of the antibacterial activity. In *Multidisciplinary Digital Publishing Institute Proceedings*.

Mortezagholi, B. *et al.* 2022 Plant-mediated synthesis of silver-doped zinc oxide nanoparticles and evaluation of their antimicrobial activity against bacteria cause tooth decay. *Microscopy Research and Technique*.

Mostafa, A. A.-F. *et al.* 2020 In vitro evaluation of antifungal activity of some agricultural fungicides against two saprolegnoid fungi infecting cultured fish. *Journal of King Saud University-Science* **32** (7), 3091–3096.

Mythili, R. *et al.* 2018a Utilization of market vegetable waste for silver nanoparticle synthesis and its antibacterial activity. *Materials Letters* **225**, 101–104.

Mythili, R. *et al.* 2018b Biogenic synthesis, characterization and antibacterial activity of gold nanoparticles synthesised from vegetable waste. *Journal of Molecular Liquids* **262**, 318–321.

Naveenraj, S. *et al.* 2018 A general microwave synthesis of metal (Ni, Cu, Zn) selenide nanoparticles and their competitive interaction with human serum albumin. *New Journal of Chemistry* **42** (8), 5759–5766.

Nazaripour, E. *et al.* 2022 Ferromagnetic nickel (II) oxide (NiO) nanoparticles: biosynthesis, characterization and their antibacterial activities. *Rendiconti Lincei. Scienze Fisiche e Naturali* **33** (1), 127–134.

Nazari-Vanani, R. *et al.* 2019 Electrochemical biosensing of 16s rRNA gene sequence of Enterococcus faecalis. *Biosensors and Bioelectronics* **142**, 111541.

Nazeer, M. *et al.* 2022 Theoretical study of MHD electro-osmotically flow of third-grade fluid in micro channel. *Applied Mathematics and Computation* **420**, 126868.

Nguyen, M. B. *et al.* 2021 Bimetallic Ag-Zn-BTC/GO composite as highly efficient photocatalyst in the photocatalytic degradation of reactive yellow 145 dye in water. *Journal of Hazardous Materials* **420**, 126560.

Obireddy, S. R. & Lai, W.-F. 2021 Preparation and characterization of 2-hydroxyethyl starch microparticles for co-delivery of multiple bioactive agents. *Drug Delivery* **28** (1), 1562–1568.

Opelt, S. *et al.* 2008 Preparation of palladium supported on MOF-5 and its use as hydrogenation catalyst. *Catalysis Communications* **9** (6), 1286–1290.

Park, J. *et al.* 2016 Size-controlled synthesis of porphyrinic metal–organic framework and functionalization for targeted photodynamic therapy. *Journal of the American Chemical Society* **138** (10), 3518–3525.

Patel, P. *et al.* 2018 Amine-functionalized Zn (II) MOF as an efficient multifunctional catalyst for CO 2 utilization and sulfoxidation reaction. *Dalton Transactions* **47** (24), 8041–8051.

Patil, N. N. & Shukla, S. R. 2015 Degradation of Reactive Yellow 145 dye by persulfate using microwave and conventional heating. *Journal of Water Process Engineering* **7**, 314–327.

Qian, W. *et al.* 2022 Sharp inequalities for the Toader mean of order− 1 in terms of other bivariate means. *Journal of Mathematical Inequalities* **16** (1), 127–141.

Qin, Y. *et al.* 2022 Methane emission reduction and biological characteristics of landfill cover soil amended with hydrophobic biochar. *Frontiers in Bioengineering and Biotechnology* **10**.

Rabiee, N. *et al.* 2021 Diatoms with invaluable applications in nanotechnology, biotechnology, and biomedicine: recent advances. *ACS Biomaterials Science & Engineering*.

Raeisi, M. *et al.* 2021 Magnetic cobalt oxide nanosheets: green synthesis and in vitro cytotoxicity. *Bioprocess and Biosystems Engineering*.

Rafatullah, M. *et al.* 2010 Adsorption of methylene blue on low-cost adsorbents: a review. *Journal of Hazardous Materials* **177** (1–3), 70–80.

Rahim, M. *et al.* 2018 Nutratherapeutics approach against cancer: tomato-mediated synthesised gold nanoparticles. *IET Nanobiotechnology* **12** (1), 1–5.

Rajabizadeh, A. *et al.* 2022 The recent advances of metal–organic frameworks in electric vehicle batteries. *Journal of Inorganic and Organometallic Polymers and Materials*.

Rajadurai, U. M. *et al.* 2021 Assessment of behavioral changes and antitumor effects of silver nanoparticles synthesized using diosgenin in mice model. *Journal of Drug Delivery Science and Technology* **66**, 102766.

Rani, S. & Kataria, N. 2021 Metal – organic framework and its nanocomposites as chemical sensors. In: *Metal− Organic Frameworks for Environmental Sensing*. ACS Publications, pp. 83–124.

Rao, M. P. *et al.* 2018 Synthesis of N-doped potassium tantalate perovskite material for environmental applications. *Journal of Solid State Chemistry* **258**, 647–655.

Rashid, S. *et al.* 2021 New developments in weighted n-fold type inequalities via discrete generalized $\hbar^{\wedge}$ -proportional fractional operators. *Fractals*.

Rashid, S. *et al.* 2022a Some further extensions considering discrete proportional fractional operators. *Fractals* **30** (01), 2240026.

Rashid, S. *et al.* 2022b Some recent developments on dynamical discrete fractional type inequalities in the frame of nonsingular and nonlocal kernels. *Fractals* **30** (2), 2240110.

Rezapour, M. *et al.* 2021 Typologies of posttraumatic stress disorder in the Bam adult population: 17 years after Bam earthquake. *Illness, Crisis & Loss*, 10541373211054405.

Ribeiro, R. P., Esteves, I. A. & Mota, J. P. 2021 Adsorption of carbon dioxide, methane, and nitrogen on Zn (dcpa) metal-organic framework. *Energies* **14** (18), 5598.

Roostaee, M. & Sheikhshoaie, I. 2020 Magnetic nanoparticles; synthesis, properties and electrochemical application: a review. *Current Biochemical Engineering* **6** (2), 91–102.

Roostaee, M. & Sheikhshoaie, I. 2022a Low-temperature synthesis of hetero-structures of magnetically separable iron oxide@ Au-rGO nanocomposite for efficient degradation of organic dye under visible light irradiation. *Environmental Research* **205**, 112510.

Roostaee, M. & Sheikhshoaie, I. 2022b A novel, sensitive and selective nanosensor based on graphene nanoribbon–cobalt ferrite nanocomposite and 1-methyl-3-butylimidazolium bromide for detection of vanillin in real food samples. *Journal of Food Measurement and Characterization* **16** (1), 523–532.

Roostaee, M. & Sheikhshoaie, I. 2022c Fabrication of a sensitive sensor for determination of xanthine in the presence of uric acid and ascorbic acid by modifying a carbon paste sensor with Fe3O4@ Au core–shell and an ionic liquid. *Journal of Food Measurement and Characterization* **16** (1), 731–739.

Roostaee, M., Sheikhshoaei, I. & Karimi-Maleh, H. 2022 Fe3O4@ Au-rGO nanocomposite/ionic liquid modified sensor for ultrasensitive and selective sensing of doxorubicin. *Topics in Catalysis*, 1–10.

Rosales-Vázquez, L. D. *et al.* 2020 Structure of a luminescent MOF-2 derivative with a core of Zn (II)-terephthalate-isoquinoline and its application in sensing of xylenes. *Crystals* **10** (5), 344.

Sabet, S. M. *et al.* 2016 A facile approach to the synthesis of multi-walled carbon nanotube-polyhedral oligomeric silsesquioxane (POSS) nanohybrids. *Materials Letters* **168**, 9–12.

Sabouni, R., Kazemian, H. & Rohani, S. 2010 A novel combined manufacturing technique for rapid production of IRMOF-1 using ultrasound and microwave energies. *Chemical Engineering Journal* **165** (3), 966–973.

Sadeghi, H. *et al.* 2022 Iron oxyhydroxide nanoparticles: green synthesis and their cytotoxicity activity against a549 human lung adenocarcinoma cells. *Rendiconti Lincei. Scienze Fisiche e Naturali* **33** (2), 461–469.

Safaei, M. *et al.* 2019 A review on metal-organic frameworks: synthesis and applications. *TrAC Trends in Analytical Chemistry* **118**, 401–425.

Salahdin, O. D. *et al.* 2022 Oxygen reduction reaction on metal-doped nanotubes and nanocages for fuel cells. *Ionics*, 1–11.

Salarpour, S. *et al.* 2022 The application of exosomes and exosome-nanoparticle in treating brain disorders. *Journal of Molecular Liquids*, 118549.

Saravanan, M. *et al.* 2018 Green synthesis of anisotropic zinc oxide nanoparticles with antibacterial and cytofriendly properties. *Microbial Pathogenesis* **115**, 57–63.

Sargazi, S. *et al.* 2021 Synthesis, characterization, toxicity and morphology assessments of newly prepared microemulsion systems for delivery of valproic acid. *Journal of Molecular Liquids* **338**, 116625.

Sarika, K. *et al.* 2021 Antimicrobial and antifungal activity of soil actinomycetes isolated from coal mine sites. *Saudi Journal of Biological Sciences* **28** (6), 3553–3558.

Sarkar, A. *et al.* 2020 Zn-BTC MOF as an adsorbent for iodine uptake and organic dye degradation. *Crystal Growth & Design* **20** (12), 7833–7839.

Schweighauser, L., Harano, K. & Nakamura, E. 2017 Experimental study on interconversion between cubic MOF-5 and square MOF-2 arrays. *Inorganic Chemistry Communications* **84**, 1–4.

Selvam, K. *et al.* 2022 Laccase production from Bacillus aestuarii KSK using Borassus flabellifer empty fruit bunch waste as a substrate and assessing their malachite green dye degradation. *Journal of Applied Microbiology*.

Senthil, R. A. *et al.* 2019 A facile hydrothermal synthesis of visible-light responsive BiFeWO6/mos2 composite as superior photocatalyst for degradation of organic pollutants. *Ceramics International* **45** (15), 18683–18690.

Shafiee, A. *et al.* 2022 Core–shell nanophotocatalysts: review of materials and applications. *ACS Applied Nano Materials* **5** (1), 55–86.

Shen, J. *et al.* 2018 Efficient adsorption of Pb (II) from aqueous solutions by metal organic framework (Zn-BDC) coated magnetic montmorillonite. *Polymers* **10** (12), 1383.

Sindhu, T., Pavithran, R. & Vidhya, A. 2021 Design of 3D-supramolecular metal organic framework of zinc as photocatalyst for the degradation of methylene blue through advanced oxidation process. *Journal of Molecular Structure* **1245**, 131039.

Son, W.-J. *et al.* 2008 Sonochemical synthesis of MOF-5. *Chemical Communications* **47**, 6336–6338.

Sonbol, H. *et al.* 2021a Bioinspired synthesize of CuO nanoparticles using Cylindrospermum stagnale for antibacterial, anticancer and larvicidal applications. *Applied Nanoscience*, 1–11.

Sonbol, H. *et al.* 2021b Padina boryana mediated green synthesis of crystalline palladium nanoparticles as potential nanodrug against multidrug resistant bacteria and cancer cells. *Scientific Reports* **11** (1), 1–19.

Soni, S. *et al.* 2020a Utilisation of cobalt doped iron based MOF for enhanced removal and recovery of methylene blue dye from waste water. *Journal of Molecular Liquids* **314**, 113642.

Soni, S. *et al.* 2020b Removal of crystal violet from aqueous solution using iron based metal organic framework. *Desalination and Water Treatment* **205**, 386–399.

Stock, N. & Biswas, S. 2012 Synthesis of metal-organic frameworks (MOFs): routes to various MOF topologies, morphologies, and composites. *Chemical Reviews* **112** (2), 933–969.

Subramaniyan, S. B. *et al.* 2022 Phytolectin-cationic lipid complex revive ciprofloxacin efficacy against multi-drug resistant uropathogenic Escherichia coli. *Colloids and Surfaces A: Physicochemical and Engineering Aspects* **647**, 128970.

Sumida, K. *et al.* 2017 Sol–gel processing of metal–organic frameworks. *Chemistry of Materials* **29** (7), 2626–2645.

Surib, N. A. *et al.* 2017 Ag + , Fe 3 + and Zn 2 + -intercalated cadmium (ii)-metal–organic frameworks for enhanced daylight photocatalysis. *RSC Advances* **7** (81), 51272–51280.

Swathi, S. *et al.* 2020 Cancer targeting potential of bioinspired chain like magnetite (Fe3O4) nanostructures. *Current Applied Physics* **20** (8), 982–987.

Talha, K. *et al.* 2021 Construction of a mixed ligand MOF as 'green catalyst' for the photocatalytic degradation of organic dye in aqueous media. *RSC Advances* **11** (38), 23838–23845.

Tan, Z.-R. *et al.* 2022a EDOT-based conjugated polymers accessed via C–H direct arylation for efficient photocatalytic hydrogen production. *Chemical Science*.

Tan, Z. *et al.* 2022b Electric field applications enhance the electron transfer capacity of dissolved organic matter in sludge compost. *Environmental Technology*, 1–22.

Tan, Z. *et al.* 2022c Effect of ventilation quantity on electron transfer capacity and spectral characteristics of humic substances during sludge composting. *Environmental Science and Pollution Research*, 1–16.

Tian, H. *et al.* 2021a Summer maize mapping by compositing time series sentinel-1A imagery based on crop growth cycles. *Journal of the Indian Society of Remote Sensing* **49** (11), 2863–2874.

Tian, H. *et al.* 2021b Early-season mapping of winter crops using sentinel-2 optical imagery. *Remote Sensing* **13** (19), 3822.

Tian, H.-X. *et al.* 2021c Metal-organic frameworks based on tetra (imidazole) and multicarboxylate: syntheses, structures, luminescence, photocatalytic and sonocatalytic degradation of methylene blue. *Polyhedron* **197**, 115052.

Uddin, M. J., Ampiaw, R. E. & Lee, W. 2021 Adsorptive removal of dyes from wastewater using a metal-organic framework: a review. *Chemosphere* **284**, 131314.

Valarmathi, N. *et al.* 2020 Utilization of marine seaweed Spyridia filamentosa for silver nanoparticles synthesis and its clinical applications. *Materials Letters* **263**, 127244.

Vidhya, M. S. *et al.* 2021 Anti-cancer applications of Zr, Co, Ni-doped ZnO thin nanoplates. *Materials Letters* **283**, 128760.

Volodymyr, A., Sergii, K. & Kozyk, O. 2021 Evaluation of the effectiveness of mini-screw-facilitated micro-osteoperforation interventions on the treatment process in patients with orthodontic treatment: a systematic review and meta-analysis. *International Journal of Scientific Research in Dental and Medical Sciences* **3** (3), 147–152.

Wang, X.-L. *et al.* 2017 Four thiophene-pyridyl-amide-based ZnII/CdII coordination polymers: assembly, structures, photocatalytic properties and fluorescent recognition for Fe3 + . *Journal of Solid State Chemistry* **249**, 51–57.

Wang, J.-J. *et al.* 2018a Selective fluorescent sensing and photocatalytic properties of zinc (II) and cadmium (II) coordination architectures with naphthalene-1, 5-disulfonate and 2, 4, 5-tri (4-pyridyl)-imidazole. *Inorganica Chimica Acta* **482**, 447–453.

Wang, D. *et al.* 2018b MOF-derived Zn–Mn mixed oxides@ carbon hollow disks with robust hierarchical structure for high-performance lithium-ion batteries. *Journal of Materials Chemistry A* **6** (7), 2974–2983.

Wang, M.-K. *et al.* 2020 Inequalities for generalized trigonometric and hyperbolic functions with one parameter. *Journal of Mathematical Inequalities* **14** (1), 1–21.

Wang, X. *et al.* 2021a Radium and nitrogen isotopes tracing fluxes and sources of submarine groundwater discharge driven nitrate in an urbanized coastal area. *Science of The Total Environment* **763**, 144616.

Wang, J. *et al.* 2021b A donor–acceptor liganded metal–organic framework showcases the hydrogen-bond-enhanced sensing of N-heterocyclic explosives. *Journal of Materials Chemistry C* **9** (36), 12086–12093.

Wang, J. *et al.* 2021c Two 3D supramolecular isomeric Zn (II)-MOFs as photocatalysts for photodegradation of methyl violet dye. *Dyes and Pigments* **190**, 109285.

Wang, Q. *et al.* 2022a Tourmaline enhanced methane yield via regulating microbial metabolic balance during anaerobic co-digestion of corn stover and cow manure. *Bioresource Technology* **359**, 127470.

Wang, Y. *et al.* 2022b Mo-modified band structure and enhanced photocatalytic properties of tin oxide quantum dots for visible-light driven degradation of antibiotic contaminants. *Journal of Environmental Chemical Engineering* **10** (1), 107091.

Wang, Q. *et al.* 2022c Co-hydrothermal carbonization of organic solid wastes to hydrochar as potential fuel: a review. *Science of The Total Environment* 158034.

Wang, F. *et al.* 2022d Numerical solution of traveling waves in chemical kinetics: time-fractional fishers equations. *Fractals* **30** (02), 2240051.

Wang, L. *et al.* 2022e A novel core-shell structured hybrid composed of zinc homobenzotrizoate and silver borotungstate with supercapacitor and photocatalytic dye degradation performance. *Journal of Energy Storage* **46**, 103873.

Wei, Y.-P. *et al.* 2020 An electrochemiluminescence biosensor for p53 antibody based on Zn-MOF/GO nanocomposite and Ag + -DNA amplification. *Microchimica Acta* **187** (8), 1–9.

Wen, X.-J. *et al.* 2020 Photocatalytic degradation of sulfamethazine using a direct Z-Scheme AgI/Bi4V2O11 photocatalyst: mineralization activity, degradation pathways and promoted charge separation mechanism. *Journal of Hazardous Materials* **385**, 121508.

Wiwasuku, T. *et al.* 2020 Sonochemical synthesis of microscale Zn (ii)-MOF with dual Lewis basic sites for fluorescent turn-on detection of Al^{3+} and methanol with low detection limits. *Dalton Transactions* **49** (29), 10240–10249.

Wu, X. *et al.* 2021 Circulating purification of cutting fluid: an overview. *The International Journal of Advanced Manufacturing Technology* **117** (9), 2565–2600.

Xia, J., Majdi, A. & Toghraie, D. 2022 Molecular dynamics simulation of friction process in atomic structures with spherical nanoparticles. *Solid State Communications* **346**, 114717.

Xin, C. *et al.* 2021 Minimum quantity lubrication machining of aeronautical materials using carbon group nanolubricant: from mechanisms to application. *Chinese Journal of Aeronautics*.

Xu, H.-Z., Qian, W.-M. & Chu, Y.-M. 2022 Sharp bounds for the lemniscatic mean by the one-parameter geometric and quadratic means. *Revista de la Real Academia de Ciencias Exactas, Físicas y Naturales. Serie A. Matemáticas* **116** (1), 1–15.

Xue, H. *et al.* 2022 Adsorption of methylene blue from aqueous solution on activated carbons and composite prepared from an agricultural waste biomass: a comparative study by experimental and advanced modeling analysis. *Chemical Engineering Journal* **430**, 132801.

Yadav, A. *et al.* 2022 Experimental study and numerical optimization for removal of methyl orange using polytetrafluoroethylene membranes in vacuum membrane distillation process. *Colloids and Surfaces A: Physicochemical and Engineering Aspects* **635**, 128070.

Yang, J.-M., Liu, Q. & Sun, W.-Y. 2014 Co (II)-doped MOF-5 nano/microcrystals: Solvatochromic behaviour, sensing solvent molecules and gas sorption property. *Journal of Solid State Chemistry* **218**, 50–55.

Yang, Y. *et al.* 2019a Nanoporous gold embedded ZIF composite for enhanced electrochemical nitrogen fixation. *Angewandte Chemie International Edition* **58** (43), 15362–15366.

Yang, M. *et al.* 2019b Predictive model for minimum chip thickness and size effect in single diamond grain grinding of zirconia ceramics under different lubricating conditions. *Ceramics International* **45** (12), 14908–14920.

Yang, M. *et al.* 2021a Predictive model of convective heat transfer coefficient in bone micro-grinding using nanofluid aerosol cooling. *International Communications in Heat and Mass Transfer* **125**, 105317.

Yang, Y. *et al.* 2021b Mechanical performance of 316 L stainless steel by hybrid directed energy deposition and thermal milling process. *Journal of Materials Processing Technology* **291**, 117023.

Yang, M. *et al.* 2021c Semiempirical heat flux model of hard-brittle bone material in ductile microgrinding. *Journal of Manufacturing Processes* **71**, 501–514.

Ye, J. *et al.* 2016 New metal–organic frameworks constructed by 2, 5-bis (3-pyridyl)-3, 4-diaza-2, 4-hexadiene and dicarboxylic ligands: enhanced photocatalytic effect. *Inorganic Chemistry Communications* **66**, 36–40.

Yu, Y.-Q. *et al.* 2016 A sensitive electrochemiluminescent aptasensor based on perylene derivatives as a novel co-reaction accelerator for signal amplification. *Biosensors and Bioelectronics* **85**, 8–15.

Zebardast, M., Fallah Shojaei, A. & Tabatabaeian, K. 2018 Enhanced removal of methylene blue dye by bimetallic nano-sized MOF-5s. *Iranian Journal of Catalysis* **8** (4), 297–309.

Zha, T.-H. *et al.* 2021 A fuzzy-based strategy to suppress the novel coronavirus (2019-NCOV) massive outbreak. *Applied and Computational Mathematics*, 160–176.

Zhang, X. *et al.* 2015 Fabrication of porous metal–organic frameworks via a mixed-ligand strategy for highly selective and efficient dye adsorption in aqueous solution. *CrystEngComm* **17** (31), 6037–6043.

Zhang, X. *et al.* 2017 Lubricating property of MQL grinding of Al_2O_3/SiC mixed nanofluid with different particle sizes and microtopography analysis by cross-correlation. *Precision Engineering* **47**, 532–545.
Zhang, J. *et al.* 2018a Experimental assessment of an environmentally friendly grinding process using nanofluid minimum quantity lubrication with cryogenic air. *Journal of Cleaner Production* **193**, 236–248.
Zhang, M. *et al.* 2018b Two pure MOF-photocatalysts readily prepared for the degradation of methylene blue dye under visible light. *Dalton Transactions* **47** (12), 4251–4258.
Zhang, Y. *et al.* 2018c Enhanced photocatalytic performance and degradation pathway of Rhodamine B over hierarchical double-shelled zinc nickel oxide hollow sphere heterojunction. *Applied Surface Science* **430**, 549–560.
Zhang, N. *et al.* 2020 Enhanced acetone sensing property of a sacrificial template based on cubic-like MOF-5 doped by Ni nanoparticles. *Nanomaterials* **10** (2), 386.
Zhang, L. *et al.* 2021a Effects of coexisting Na^+, Mg^{2+} and Fe^{3+} on nitrogen and phosphorus removal and sludge properties using A2O process. *Journal of Water Process Engineering* **44**, 102368.
Zhang, Z. *et al.* 2021b Metal–organic frameworks (MOFs) based chemosensors/biosensors for analysis of food contaminants. *Trends in Food Science & Technology* **118**, 569–588.
Zhang, Y. *et al.* 2022 Nano-enhanced biolubricant in sustainable manufacturing: from processability to mechanisms. *Friction*, 1–39.
Zhao, H. *et al.* 2018a Synthesis and characterization of Zn 2 GeO_4/Mg-MOF-74 composites with enhanced photocatalytic activity for CO_2 reduction. *Catalysis Science & Technology* **8** (5), 1288–1295.
Zhao, T.-H. *et al.* 2018b Quadratic transformation inequalities for Gaussian hypergeometric function. *Journal of Inequalities and Applications* **2018** (1), 1–15.
Zhao, T.-H. *et al.* 2019 On approximating the quasi-arithmetic mean. *Journal of Inequalities and Applications* **2019** (1), 1–12.
Zhao, T.-H., He, Z.-Y. & Chu, Y.-M. 2020a On some refinements for inequalities involving zero-balanced hypergeometric function. *AIMS Math* **5** (6), 6479–6495.
Zhao, T.-H., Wang, M.-K. & Chu, Y.-M. 2020b A sharp double inequality involving generalized complete elliptic integral of the first kind. *AIMS Math* **5** (5), 4512–4528.
Zhao, T.-H., Shi, L. & Chu, Y.-M. 2020c Convexity and concavity of the modified Bessel functions of the first kind with respect to Hölder means. *Revista de la Real Academia de Ciencias Exactas, Físicas y Naturales. Serie A. Matemáticas* **114** (2), 1–14.
Zhao, T. H., Khan, M. I. & Chu, Y. M. 2021a Artificial neural networking (ANN) analysis for heat and entropy generation in flow of non-Newtonian fluid between two rotating disks. *Mathematical Methods in the Applied Sciences*.
Zhao, T.-H., He, Z.-Y. & Chu, Y.-M. 2021b Sharp bounds for the weighted Hölder mean of the zero-balanced generalized complete elliptic integrals. *Computational Methods and Function Theory* **21** (3), 413–426.
Zhao, T.-H., Wang, M.-K. & Chu, Y.-M. 2021c Concavity and bounds involving generalized elliptic integral of the first kind. *Journal of Mathematical Inequalities* **15** (2), 701–724.
Zhao, T.-H., Wang, M.-K. & Chu, Y.-M. 2021d Monotonicity and convexity involving generalized elliptic integral of the first kind. *Revista de la Real Academia de Ciencias Exactas, Físicas y Naturales. Serie A. Matemáticas* **115** (2), 1–13.
Zhao, T.-H., Qian, W.-M. & Chu, Y.-M. 2021e On approximating the arc lemniscate functions. *Indian Journal of Pure and Applied Mathematics* 1–14.
Zhao, T.-H., Bhayo, B. A. & Chu, Y.-M. 2021f Inequalities for generalized Grötzsch ring function. *Computational Methods and Function Theory*, 1–16.
Zhao, T.-H., Shen, Z.-H. & Chu, Y.-M. 2021g Sharp power mean bounds for the lemniscate type means. *Revista de la Real Academia de Ciencias Exactas. Físicas y Naturales. Serie A. Matemáticas* **115** (4), 1–16.
Zhao, T.-H., Qian, W.-M. & Chu, Y.-M. 2021h Sharp power mean bounds for the tangent and hyperbolic sine means. *Journal of Mathematical Inequalities* **15** (4), 1459–1472.
Zhao, T., Wang, M. & Chu, Y. 2022a On the bounds of the perimeter of an ellipse. *Acta Mathematica Scientia* **42** (2), 491–501.
Zhao, T.-H. *et al.* 2022b Landen inequalities for Gaussian hypergeometric function. *Revista de la Real Academia de Ciencias Exactas, Físicas y Naturales. Serie A. Matemáticas* **116** (1), 1–23.
Zhao, T.-H., Chu, H.-H. & Chu, Y.-M. 2022c Optimal Lehmer mean bounds for the nth power–type Toader means of $n = -$ 1, 1, 3. 2022, element r Austrije 11, 10000 Zagreb, Croatia. 157–159.
Zhao, T.-H. *et al.* 2022d On the generalized power–type Toader mean. *Journal of Mathematical Inequalities* **16** (1), 247–249.
Zheng, J. *et al.* 2022 Photoclick reaction constructs Glutathione-Responsive Theranostic System for anti-tuberculosis. *Frontiers in Molecular Biosciences* **9**.
Zhu, L. *et al.* 2022 A new strategy for the development of efficient impedimetric tobramycin aptasensors with metallo-covalent organic frameworks (MCOFs). *Food Chemistry* **366**, 130575.

First received 19 July 2022; accepted in revised form 3 October 2022. Available online 11 October 2022